WCDA Regularization for 3D Quantitative Microwave Tomography

Funing Bai[1], Aleksandra Pižurica[1], Bart Truyen[2], Wilfried Philips[1] and Ann Franchois[3]

[1]Department of Telecommunications and Information Processing (TELIN-IPI-iminds), Ghent University, B-9000, Ghent, Belgium

[2] Department of Electronics and Informatics (ETRO), Vrije Universiteit Brussel, Brussels, Belgium

[3]Department of Information Technology (INTEC), Ghent University, B-9000, Ghent, Belgium

E-mail: Funing.Bai@telin.ugent.be

Abstract. We present an analysis of weakly convex discontinuity adaptive (WCDA) models for regularizing three-dimensional (3D) quantitative microwave imaging. In particular, we are concerned with complex permittivity reconstructions from sparse measurements such that the reconstruction process is significantly accelerated. When dealing with such highly underdetermined problem, it is crucial to employ regularization, relying in this case on prior knowledge about the structural properties of the underlying permittivity profile: we consider piecewise homogeneous objects. We present a numerical study on the choice of the potential function parameter for the Huber function and for two selected WCDA functions, one of which (Leclerc - Cauchy-Lorentzian) is designed to be more edge-preserving than the other (Leclerc - Huber). We evaluate the effect of reducing the number of (simulated) scattered field data on the reconstruction quality. Furthermore, reconstructions from sub-sampled single-frequency experimental data from the 3D Fresnel database illustrate the effectiveness of WCDA regularization.

1. Introduction

Microwave Imaging computes internal sections of objects using microwaves [1]. The images are obtained by processing the data collected by illuminating the object with known incident fields and by measuring the scattered fields. Quantitative Microwave Imaging (QMI) aims at estimating the exact complex permittivity profile of the object. Due to its non-invasive nature, this imaging modality is of interest in biomedical imaging [2], subsurface imaging [3] and for civil and industrial applications [4].

The problem of QMI is challenging because the measured data samples of the scattered fields are related to the unknowns (the tomographic image samples) through a non-linear mapping [5]. Employing appropriate optimization techniques, such as Newton-type methods [6–10], may address the non-linearity of the problem. The problem is also ill-posed [11] and regularization is required to improve the convergence and stability by reducing the solution space.

A number of regularization methods have been analyzed in the setting of QMI, e.g. [12–18]. Total variation (TV) and weighted L2-norm TV are applied as a multiplicative constraint in [12] and [13], respectively. Edge preserving regularization was imposed on the real and imaginary parts of the complex permittivity separately in [14]. Multiplicative Smoothing (MS) [10, 15] applies quadratic regularization in a multiplicative fashion. Value Picking (VP) was proposed in [16] as a non-spatial technique that favors solutions consisting of piecewise constant permittivities while Piecewise Smoothed Value Picking [17] includes an additional smoothing regularizer. A Markov Random Field (MRF) regularization with Line Process (LP) model was employed in [18] and with weak membrane model in [19]. Some of the authors of this paper analyzed the use of robust Huber regularization [20] and recently proposed a class of Weakly Convex Discontinuity Adaptive (WCDA) regularizing functions for 2D QMI [21]. These functions conform to the definition of discontinuity adaptive (DA) MRF's while having a highly sensitive adaptive interaction function (AIF) [22] and are designed to allow convex optimization in the framework of a (modified) Gauss-Newton algorithm.

The work presented in this paper builds further on the ideas of WCDA regularization presented in [21], but reconstruction in 3D that we address here is more challenging. Our focus is on piecewise constant 3D objects and we employ dimensions of the order of a (few) wavelength(s). The main contributions are the following: Firstly, we analyze the properties of different WCDA functions, including the Huber regularizer employed in [20], and we discuss their incorporation into the Gauss-Newton algorithm. We investigate by means of simulations the influence of the function parameter on the reconstruction quality for some 3D test objects, applying various antenna configurations and noise levels. Secondly, we apply these methods to experimental data from the 3D Fresnel database [23] and compare their behavior to other related regularization methods in this context [24]. Thirdly, we consider sparse reconstructions, meaning that the number of scattered field data is small compared to the number of unknown permittivity cells, employing different data subsampling strategies (uniformly versus non uniformly distributed transmitters) and analyzing the effect of this subsampling on the reconstruction results. We use single-frequency data and far less transmitters and receivers than available in the Fresnel database, since we are interested to explore potentials of WCDA regularization for compensating for the underdetermined problem while speeding up the reconstruction process.

The paper is organized as follows. In Section 2, the electromagnetic inverse scattering problem and optimization process are described. The basic theory of MRF and Discontinuity Adaptive models is reviewed briefly in Section 3 and the WCDA class of models is discussed in Section 4. Sections 5 and 6 are devoted to validation on simulated and experimental data, respectively, and Section 7 concludes the paper.

2. The Electromagnetic Inverse Scattering Problem

Assume an unknown 3D object surrounded with a known homogeneous medium and contained in a reconstruction domain $\mathcal{D}$, that is a rectangular cuboid centered in the origin of the coordinate system. Our goal is to reconstruct the relative complex permittivity $\varepsilon(\boldsymbol{r}) = \varepsilon'(\boldsymbol{r}) + j\varepsilon''(\boldsymbol{r})$ in every point $\boldsymbol{r}$ in $\mathcal{D}$. We shall consider multi-view microwave illuminations at a single frequency f. The time dependency $e^{j\omega t}$ of the fields will be omitted.

2.1. Forward Problem

In the forward model, the complex permittivity profile is specified in $\mathcal{D}$ and the incident electrical field $\boldsymbol{E}_i^{inc}$ (the index i labels the transmitter position and polarization) is modeled as an elementary dipole field

$$\boldsymbol{E}_i^{inc}(\boldsymbol{r}) = -j\omega\mu_0 \boldsymbol{G}_b(\boldsymbol{r} - \boldsymbol{r}_i) \cdot \hat{\boldsymbol{u}}_i \tag{1}$$

where μ_0 is the permeability of vacuum and where $\boldsymbol{r}_i$ and the unit vector $\hat{\boldsymbol{u}}_i$ denote the position and the orientation of the i-th elementary dipole, respectively. $\boldsymbol{G}_b$ is the Green dyadic of homogeneous space with relative permittivity ε_b, i.e.

$$\boldsymbol{G}_b(\boldsymbol{r}, \boldsymbol{r}') = \left[\mathbf{I} + \frac{\nabla\nabla}{k_b^2}\right] G_b(\boldsymbol{r} - \boldsymbol{r}') \tag{2}$$

where $k_b = \omega\sqrt{\varepsilon_b \varepsilon_0 \mu_0}$ is the propagation constant of the background medium, ε_0 is the permittivity of vacuum, $\mathbf{I}$ is the 3×3 identity matrix and

$$G_b(\boldsymbol{r} - \boldsymbol{r}') = \frac{e^{-jk_b\|\boldsymbol{r}-\boldsymbol{r}'\|}}{4\pi\|\boldsymbol{r} - \boldsymbol{r}'\|} \tag{3}$$

is the scalar Green's function. For each incident field, the unknown scattered field is computed at the detector positions $\boldsymbol{r}_l$, which are located outside $\mathcal{D}$, as

$$\boldsymbol{E}_i^{scat}(\boldsymbol{r}_l) = \boldsymbol{E}_i(\boldsymbol{r}_l) - \boldsymbol{E}_i^{inc}(\boldsymbol{r}_l) \tag{4}$$

with $\boldsymbol{E}_i(\boldsymbol{r}_l)$ the total field. Since all examples in Sections 4 - 6 concern objects in free space, we put $\varepsilon_b = 1$, i.e. the relative permittivity of vacuum.

Our forward solver [10, 25] relies on a Method of Moments discretization of a mixed potential volume integral equation for the electric flux density in $\mathcal{D}$ and solves the resulting linear system iteratively with the stabilized bi-conjugate gradient Fast Fourier transform technique (BICGSTAB-FFT) [26]. This involves a discretization of the permittivity on a uniform (forward) grid that covers $\mathcal{D}$.

2.2. Inverse Problem

In the inversion the incident field (1) and measurements (experimental or simulated) of the scattered field (4) are provided. Note that in an experiment two separate measurement series are performed, one without the scatterer, yielding $\boldsymbol{E}_i^{inc}(\boldsymbol{r}_l)$ and one with the scatterer in place, yielding $\boldsymbol{E}_i(\boldsymbol{r}_l)$. The unknown permittivity $\boldsymbol{\varepsilon}(\boldsymbol{r})$ is assumed to be constant in each cubic cell of a uniform (inverse) grid that covers $\mathcal{D}$, resulting in $N^{\boldsymbol{\varepsilon}}$ reconstruction variables. These are arranged in the relative complex permittivity vector $\boldsymbol{\varepsilon} = [\varepsilon_1, \cdots, \varepsilon_\nu, \cdots, \varepsilon_{N^{\varepsilon}}]$, which is updated in an iterative way, alternating between the forward and the update problem. The inverse problem is solved by iterative minimization of a cost function

$$F(\boldsymbol{\varepsilon}) = F^{LS}(\boldsymbol{\varepsilon}) + \mu F^D(\boldsymbol{\varepsilon}) \tag{5}$$

where $F^D(\boldsymbol{\varepsilon})$ denotes the regularization function, μ is a positive regularization parameter and $F^{LS}(\boldsymbol{\varepsilon})$ is the normalized least squares error between the simulated and the measured scattered fields

$$F^{LS}(\boldsymbol{\varepsilon}) = \tfrac{1}{\|\boldsymbol{e}^{meas}\|^2} \|\boldsymbol{e}^{meas} - \boldsymbol{e}^{scat}(\boldsymbol{\varepsilon})\|^2 \tag{6}$$

where $\boldsymbol{e}^{scat}(\boldsymbol{\varepsilon})$ and $\boldsymbol{e}^{meas}$ are two N^d-dimensional vectors, which contain the components of, respectively, the scattered field vectors $\boldsymbol{E}_i^{scat}(\boldsymbol{r}_l)$ computed for the current permittivity vector $\boldsymbol{\varepsilon}$ at the detector positions $\boldsymbol{r}_l$ for every illumination i and of the corresponding measured data $\boldsymbol{E}_i^{meas}(\boldsymbol{r}_l)$. In this paper a spherical measurement geometry is adopted and transmitting antennas are modelled as elementary dipoles (1) [10]. Suppose there are N^T transmitting positions $\boldsymbol{r}_t$ ($t = 1, \cdots, N^T$) located on a sphere with in each position two tangential transmitting polarizations: $\hat{\boldsymbol{u}}_{t,\theta}$ (polar) and $\hat{\boldsymbol{u}}_{t,\phi}$ (azimuthal). Every transmitting position is linked to a set of N_t^R receiver locations (on the same sphere as the transmitters in Sections 4 and 5; on a circle with a smaller radius in Section 6), denoted as $\boldsymbol{r}_l$ ($l = 1, \cdots, N_t^R$), and in each receiver location the scattered field can be measured along $\hat{\boldsymbol{u}}_{l,\theta}$ and $\hat{\boldsymbol{u}}_{l,\phi}$. This results in a total number of maximum $N^d = 2\sum\limits_{t=1}^{N^T} 2N_t^R$ (complex) scalar field components; in Section 6, only the $\hat{\boldsymbol{u}}_{l,\theta}$ component is available, hence $N^d = 2\sum\limits_{t=1}^{N^T} N_t^R$.

In choosing the sparse antenna configurations in Sections 4-6 we start from a setup similar to [16] for the numerical study and from the 3D Fresnel configuration [23] for the experimental study, which we both subsample in a variety of ways. It is not our aim to subsample according to the number of degrees of freedom (NDF) criterion in [27]. Some of our antenna configurations are (partially) uniform, some are aspect-limited; they provide in some cases less, in other cases more data than the corresponding NDF estimate, but the amount of unknown permittivity cells is always considerably larger than NDF.

We define the regularization function $F^D(\boldsymbol{\varepsilon})$ as

$$F^D(\boldsymbol{\varepsilon}) = \tfrac{1}{2} \sum_{\nu} \sum_{\nu' \in N_\nu} g_\gamma(\varepsilon_\nu - \varepsilon_{\nu'}) \tag{7}$$

where g_γ is a real function with parameter γ. The index ν' denotes a spatial position (a discretization cell of the inverse grid) neighboring ν in the neighborhood N_ν. We use 26 neighbors in 3D as a compromise between reconstruction quality and complexity. The normalization factor $\frac{1}{2}$ accounts for the duality of neighbors, which follows from the symmetry of N_ν and from the even property of g, i.e. $g(\varepsilon_{\nu'} - \varepsilon_\nu) = g(\varepsilon_\nu - \varepsilon_{\nu'})$.

Algorithm 1 The algorithm for reconstructing $\boldsymbol{\varepsilon}$

Require: $\boldsymbol{\varepsilon}_{init}$, μ, γ, $\boldsymbol{e}^{meas}$
  $k = 0$
  $\boldsymbol{\varepsilon}_k \leftarrow \boldsymbol{\varepsilon}_{init}$
  Compute $\lambda^2 = \mu \|\boldsymbol{e}^{meas}\|^2$
  repeat
    Compute $\boldsymbol{e}^{scat}(\boldsymbol{\varepsilon}_k)$
    if $\frac{\|\boldsymbol{e}^{scat}(\boldsymbol{\varepsilon}_k) - \boldsymbol{e}^{meas}\|^2}{\|\boldsymbol{e}^{meas}\|^2} < 10^{-3}$ **then**
      return $\boldsymbol{\varepsilon}_k$
    else
      Compute $\mathbf{J}_k$, $\mathbf{J}_k^H$, $\boldsymbol{\Omega}_k^{D*}$ and $\boldsymbol{\Sigma}_k^D$
      Compute $\boldsymbol{\Delta\varepsilon}_k$ using (8)
      Compute β_k with line search
      $\boldsymbol{\varepsilon}_{k+1} = \boldsymbol{\varepsilon}_k + \beta_k \boldsymbol{\Delta\varepsilon}_k$
      $k = k + 1$
    end if
  until $k =$ The maximum number of iterations
  print $\boldsymbol{\varepsilon}_k$

2.3. Optimization Algorithm

For the minimization of (5) we apply a Newton-type method, where we employ the (independent) variables ε_ν and ε_ν^* (similar to [28]), where $(.)^*$ denotes the complex conjugate. The complex permittivity in iteration k is updated as $\boldsymbol{\varepsilon}_{k+1} = \boldsymbol{\varepsilon}_k + \beta_k \boldsymbol{\Delta\varepsilon}_k$, where $\boldsymbol{\Delta\varepsilon}_k$ is a (modified) Gauss-Newton step, which is used as a search direction along which β_k approximately minimizes the cost function $F(\boldsymbol{\varepsilon})$ [16]. By applying the Newton update formula to (5) and neglecting certain second-order derivations ($\frac{\partial^2}{\partial\varepsilon_\nu \partial\varepsilon_{\nu'}}$ and $\frac{\partial^2}{\partial\varepsilon_\nu^* \partial\varepsilon_{\nu'}^*}$) in the complex Hessian matrix $\mathbf{H} = \mathbf{H}^{LS} + \mu \mathbf{H}^D$, the update direction is obtained from

$$(\mathbf{J}_k^H \mathbf{J}_k + \lambda^2 \boldsymbol{\Sigma}_k^D)\boldsymbol{\Delta\varepsilon}_k = -(\mathbf{J}_k^H[\boldsymbol{e}^{scat}(\boldsymbol{\varepsilon}_k) - \boldsymbol{e}^{meas}] + \lambda^2 \boldsymbol{\Omega}_k^{D*}) \tag{8}$$

where $(.)^H$ stands for Hermitian transpose and the trade-off parameter λ is given by $\lambda^2 = \mu \|\boldsymbol{e}^{meas}\|^2$. The subscript k is omitted in the following. $\mathbf{J}$ is the $N^d \times N^\varepsilon$ Jacobian matrix, which contains the derivatives of the scattered field components with respect to the optimization variables: $J_{d\nu} = \partial e_d^{scat} / \partial \varepsilon_\nu$. For $F^D(\boldsymbol{\varepsilon})$ the complex gradient is given by

$$\mathbf{g}^D = \begin{bmatrix} \frac{\partial F^D}{\partial \varepsilon_\nu} \\ \frac{\partial F^D}{\partial \varepsilon_\nu^*} \end{bmatrix} = \begin{bmatrix} \boldsymbol{\Omega}^D \\ \boldsymbol{\Omega}^{D*} \end{bmatrix} \tag{9}$$

where $\boldsymbol{\Omega}^{D*}$ is a N^ε-dimensional vector of the first order derivatives of $F^D(\boldsymbol{\varepsilon})$ with respect to the complex conjugate reconstruction variables ε_ν^*. The WCDA regularization functions proposed further in Section 4 are of the form $g_\gamma(\varepsilon_\nu - \varepsilon_{\nu'}) = f_\gamma(|\varepsilon_\nu - \varepsilon_{\nu'}|)$. It follows that the complex Hessian matrix of F^D is given by

$$\mathbf{H}^D = \begin{bmatrix} \frac{\partial^2 F^D}{\partial\varepsilon_{\nu'}\partial\varepsilon_\nu} & \frac{\partial^2 F^D}{\partial\varepsilon_{\nu'}\partial\varepsilon^*_\nu} \\ \\ \frac{\partial^2 F^D}{\partial\varepsilon^*_{\nu'}\partial\varepsilon_\nu} & \frac{\partial^2 F^D}{\partial\varepsilon^*_{\nu'}\partial\varepsilon^*_\nu} \end{bmatrix} = \begin{bmatrix} \boldsymbol{B}^D & \boldsymbol{\Sigma}^D \\ \\ \boldsymbol{\Sigma}^D & \boldsymbol{B}^{D*} \end{bmatrix} \tag{10}$$

where the $N^\varepsilon \times N^\varepsilon$ submatrices $\boldsymbol{\Sigma}^D$ and $\boldsymbol{B}^D$ are real symmetric and complex symmetric, respectively. With VP regularization [16], the matrix $\boldsymbol{B}^P$ is identically zero; with MS regularization [10], the matrix $\boldsymbol{B}^S$ is negligible for small contrasts (near the beginning of the iterations) and for small datafits (near convergence); with the WCDA functions proposed in Section 4, $\boldsymbol{B}^D$ is negligible for small contrasts and will be neglected in (10), thus leading to the (modified) Gauss-Newton equation (8). Whatever approximations have led to (8), it is important that the line search direction $\boldsymbol{\Delta\varepsilon}$ is a descent direction for $F(\boldsymbol{\varepsilon})$ to ensure convergence of the method, which requires that the matrix $\mathbf{J}^H\mathbf{J} + \lambda^2\boldsymbol{\Sigma}^D$ in (8) is positive definite. The diagonal elements of $\boldsymbol{\Sigma}^D$ are

$$\Sigma^D_{\nu,\nu} = \frac{\partial^2 F^D}{\partial\varepsilon_\nu\partial\varepsilon^*_\nu} = \frac{\partial^2 F^D}{\partial\varepsilon_{j,k,l}\partial\varepsilon^*_{j,k,l}} \tag{11}$$

where j, k, l label the discretization cells in the x, y, z-directions, respectively, and the non-diagonal elements are

$$\Sigma^D_{\nu,\nu'} = \frac{\partial^2 F^D}{\partial\varepsilon_{\nu'}\partial\varepsilon^*_\nu} = \frac{\partial^2 F^D}{\partial\varepsilon_{j',k',l'}\partial\varepsilon^*_{j,k,l}} \tag{12}$$

which are zero except if $\nu' \in N_\nu$. A pseudo-code of the reconstruction algorithm is given under Algorithm 1. For all examples in Sections 4 - 6, the initial permittivity estimate ε_{init} is equal to the background permittivity $\boldsymbol{\varepsilon}_{init} = [1, \cdots, 1]$.

3. Discontinuity Adaptive Models in a MRF Approach

The regularization functions that we study in this paper belong to the so-called discontinuity-adaptive Markov random field (MRF) models [29]. It is well known that MRF provides a convenient and consistent way of modeling global context in terms of local interactions between image entities (pixels, voxels, segments, etc). According to the Hammersley-Clifford theorem [22], the joint probability of a MRF is a Gibbs distribution where energy is decomposed as a sum of clique potentials. Cliques are sets of sites (pixels, voxels) that are neighbors of each other for a particular neighborhood system. In practice, only pairwise cliques are commonly used even with larger neighborhoods. In our setting, cliques are sets of two neighboring (inverse) grid cells $< \nu, \nu' >$ for the 3D neighborhood in Fig. 1 and the clique potential function $g(\varepsilon_\nu - \varepsilon_{\nu'})$ is the regularization function from (7). Actually, the cost function in (5)-(7) can be interpreted as a Bayesian Maximum a Posteriori (MAP) estimator [19] with a MRF prior on ε_ν as follows:

$$\begin{aligned}\hat{\boldsymbol{\varepsilon}} &= \arg\max_{\boldsymbol{\varepsilon}} P(\boldsymbol{\varepsilon}|\boldsymbol{e}^{meas}) = \arg\max_{\boldsymbol{\varepsilon}} P(\boldsymbol{e}^{meas}|\boldsymbol{\varepsilon})P(\boldsymbol{\varepsilon}) \\ &= \arg\max_{\boldsymbol{\varepsilon}} P(\boldsymbol{e}^{meas}|\boldsymbol{e}^{scat}(\boldsymbol{\varepsilon}))P(\boldsymbol{\varepsilon}) \end{aligned} \tag{13}$$

If the difference between the computed and measured scattered fields for each detector l and excitation i can be modeled as an independent, identically distributed Gaussian noise process $N(0, \tau^2)$, we can write:

$$\begin{aligned} P(\boldsymbol{e}^{meas}|\boldsymbol{e}^{scat}(\boldsymbol{\varepsilon})) &= \prod_{i,l} P(\boldsymbol{E}_{i,l}^{meas}|\boldsymbol{E}_{i,l}^{scat}(\boldsymbol{\varepsilon})) \\ &= \prod_{i,l} \frac{1}{\tau\sqrt{2\pi}} e^{-\frac{\|\boldsymbol{E}_{i,l}^{meas} - \boldsymbol{E}_{i,l}^{scat}(\boldsymbol{\varepsilon})\|^2}{2\tau^2}} \\ &= C e^{-\sum\limits_{i,l} \frac{\|\boldsymbol{E}_{i,l}^{meas} - \boldsymbol{E}_{i,l}^{scat}(\boldsymbol{\varepsilon})\|^2}{2\tau^2}} \end{aligned} \tag{14}$$

where C is a normalizing constant. When a MRF prior with pairwise cliques $< \nu, \nu' >$ and clique potential function g_γ is imposed on $\boldsymbol{\varepsilon}$, the prior probability is

$$P(\boldsymbol{\varepsilon}) = \frac{1}{Z} e^{-\sum\limits_{<\nu,\nu'>} g_\gamma(\varepsilon_\nu - \varepsilon_{\nu'})} \tag{15}$$

where Z is a normalization constant. By substituting (14) and (15) into (13) and taking the logarithm, we obtain

$$\hat{\boldsymbol{\varepsilon}} = \arg\min_{\boldsymbol{\varepsilon}} (\sum_{i,l} \|\boldsymbol{E}_{i,l}^{meas} - \boldsymbol{E}_{i,l}^{scat}(\boldsymbol{\varepsilon})\|^2 + \lambda \sum_{\nu} \sum_{\nu' \in N_\nu} g_\gamma(\varepsilon_\nu - \varepsilon_{\nu'})) \tag{16}$$

where λ is some positive constant. The above expression for $\hat{\boldsymbol{\varepsilon}}$ is equivalent to minimizing the cost function specified in (5)-(7).

We are concerned now with the choice of the potential function g_γ. Let us first remind some well-known potential functions in one real variable r. A Tikhonov potential function $g(r) = r^2$ penalizes small differences between neighboring values, but also smooths out true discontinuities. To overcome this, a Line Process (LP) model [30, 31] switches off the smoothing when the difference between the values in the clique exceeds a certain threshold: $g_\alpha(r) = min\{r^2, \alpha\}$, where $\alpha > 0$ is a threshold parameter. More general, Discontinuity Adaptive (DA) models [22] exist that turn off smoothing less abruptly. Formally, DA models need to satisfy

$$\lim_{r\to\infty} |g'(r)| = \lim_{r\to\infty} |2rh(r)| = C \tag{17}$$

where $C \in [0, \infty)$ is a constant. The condition above with $C = 0$ entirely prohibits smoothing at discontinuities where $r \to \infty$, while it allows limited (bounded) smoothing when $C > 0$. $h(r) = g'(r)/(2r)$ is called the adaptive interaction function (AIF). As a general rule, $h(r)$ should approach 0 as $|r|$ goes to infinity. Fig. 2 illustrates the AIF

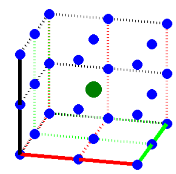

Figure 1. Neighborhood system on a lattice of regular sites

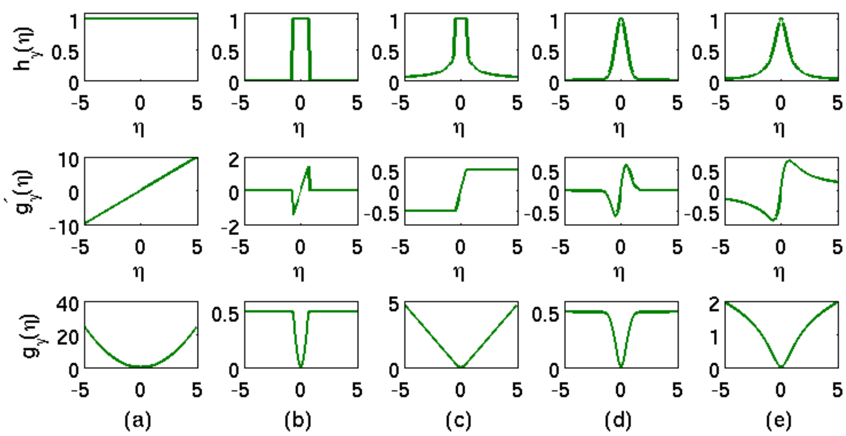

Figure 2. The qualitative shapes of Tikhonov function (a); LP model (b); Huber (c); Le Clerc (d) and Cauchy-Lorentzian function (e). The models (c) - (e) are examples of DA functions.

together with g ang g' for the Tikhonov function, LP function, Huber function [22] and two well-known more general DA models: Le Clerc [32]

$$g_l(r) = -\gamma(e^{-\frac{r^2}{\gamma}} - 1) \tag{18}$$

and Cauchy-Lorentzian [32]

$$g_c(r) = \gamma ln(1 + \tfrac{r^2}{\gamma}) \tag{19}$$

Like most other traditional DA models, (18) and (19) are convex only in an interval, where $|g^{'}(r)|$ increases monotonically with $|r|$ to smooth out the noise. Outside this interval, $|g^{'}(r)|$ decreases with $|r|$, approaching zero for large $|r|$ and the function is non-convex. Due to this problem, most of the traditional discontinuity adaptive models cannot be used in convex optimization [22].

4. Weakly Convex Discontinuity Adaptive Class of models

4.1. Formulation

Let $\eta = \alpha + j\beta$ denote a complex number, being a difference between two neighboring complex permittivities: $\eta = \varepsilon_\nu - \varepsilon_{\nu'}$. We will define here a class of discontinuity adaptive potential functions of the form $g(\eta) = f(|\eta|)$, which thus are rotationally symmetric in the complex η-plane (or in the α, β-plane). One such function is the Huber function

$$g_h(\eta) = \begin{cases} |\eta|^2 & |\eta| \leq \gamma \\ 2\gamma|\eta| - \gamma^2 & otherwise \end{cases} \tag{20}$$

which can be considered as a 2D extension of the 1D Huber model. In [20] we demonstrated the potential of Huber regularization (20) in quantitative microwave imaging, but on simulated data only and without studying its behavior thoroughly.

The Huber function yields bounded smoothing (with $C > 0$ in (17)). It is of interest to study constructions of similar models, which can potentially yield sharper edges (e.g. with $C = 0$ in (17)) or in which the AIF is made more sensitive than in the Huber function, or both. We analyze here a class of regularization functions called Weakly Convex Discontinuity Adaptive (WCDA) models that satisfy following properties [21]:

(a) Discontinuity-adaptive, i.e. condition (17) with r replaced by $|\eta|$ holds:

$$\lim_{|\eta| \to \infty} \left|\frac{dg}{d|\eta|}\right| = \lim_{|\eta| \to \infty} |2\eta h(\eta)| = C \tag{21}$$

(b) Matrix $\mathbf{\Sigma}^D$ is (semi) positive definite.

(c) Steep slope of the AIF around the origin, to make the function sensitive to subtle changes in the permittivity profile.

In particular, we can construct such WCDA models by combining two well-chosen functions (one in the origin and another one for larger values of $|\eta|$) like it is done in (20). In practice, it is convenient to start from an existing 1D DA model that is convex around the origin with a steep AIF as required in (c) and replace the tails with a function conforming to (a) - (b). We demonstrated in [21] that such construction (in this case a combination of a quadratic and a Cauchy-Lorentzian function, g_{q-c}) can be more advantageous than the Huber regularization, but there are infinitely many possible choices in this respect.

In this paper we will study constructions involving the DA functions (18) and (19), introduced in Section 3. The Le Clerc function (18) has a steep AIF so it is interesting to investigate its use in building WCDA models. Cauchy-Lorentzian (19) has the potential to better preserve sharpness of the strong edges than the Huber function, since $C = 0$ in (21), which entirely prohibits smoothing at discontinuities when $\eta \to \infty$. This also can be observed visually by comparing Figs. 2 (c) and (e). We thus construct two new functions:

$$g_{l-h}(\eta) = \begin{cases} -\gamma(e^{-\frac{|\eta|^2}{\gamma}} - 1) & |\eta| \leq \sqrt{\frac{\gamma}{2}} \\ 2\gamma|\eta| - \gamma^2 & otherwise \end{cases} \tag{22}$$

which is a combination of Le Clerc and Huber, and

$$g_{l-c}(\eta) = \begin{cases} -\gamma(e^{-\frac{|\eta|^2}{\gamma}} - 1) & |\eta| \leq \sqrt{\frac{\gamma}{2}} \\ \gamma ln(1 + \frac{|\eta|^2}{\gamma}) & otherwise \end{cases} \tag{23}$$

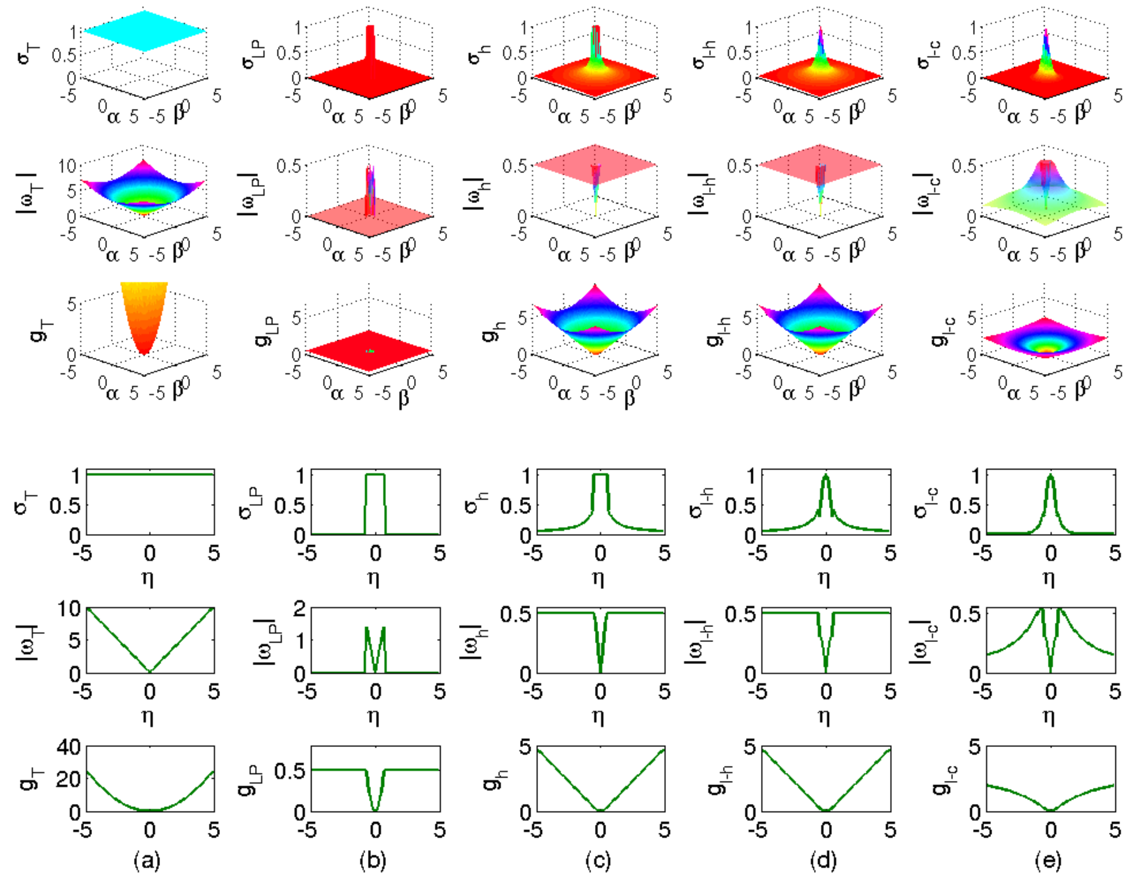

Figure 3. Qualitative 2D shapes (top) and their 1D cross sections through (0,0) (bottom) of the Tikhonov function (a), LP model (b) and WCDA functions g_h, g_{l-h} and g_{l-c} (c-e) and of their first and second order derivatives.

which combines Le Clerc with Cauchy-Lorentzian. Note that the WCDA models and/or their first derivatives can have discontinuity points, but they conform with (b) and we show that these models perform well in our optimization.

To compute $\boldsymbol{\Delta\varepsilon}_k$ in (8), the gradient and (modified) Hessian matrix of $F^D(\boldsymbol{\varepsilon})$ need to be determined. Taking into account that $|\eta|^2 = (\varepsilon_\nu - \varepsilon_{\nu'})(\varepsilon_\nu^* - \varepsilon_{\nu'}^*)$, we can express $\boldsymbol{\Omega}^{D*}$ from (9) and $\boldsymbol{\Sigma}^D$ from (11),(12) as follows:

$$\Omega_\nu^{D*} = \sum_{\nu' \in N_\nu} \omega_{\nu'} \tag{24}$$

where $\omega_{\nu'} = \frac{\partial g(\eta)}{\partial \varepsilon_\nu^*}$,

$$\Sigma_{\nu,\nu}^D = \sum_{\nu' \in N_\nu} \sigma_{\nu'} \tag{25}$$

where $\sigma_{\nu'} = \frac{\partial^2 g(\eta)}{\partial \varepsilon_\nu \partial \varepsilon_\nu^*}$ and

$$\Sigma^D_{\nu,\nu'} = -\sigma_{\nu'} \tag{26}$$

for $\nu' \in N_\nu$. The expressions of $\omega_{\nu'}$, $\sigma_{\nu'}$ and $\Sigma^D_{\nu,\nu'}$ are given in Table 1 for the Huber function (20) and for the models (22), (23). It can be seen in Table 1 that $\sigma_{\nu'}$ is always positive. From (25),(26) it then follows that $\mathbf{\Sigma}^D$ is diagonally dominant, since $|\Sigma^D_{\nu,\nu}| \geq \sum_{\nu'} |\Sigma^D_{\nu,\nu'}|$ for every row ν‡. Furthermore, all diagonal entries (25) are positive. It follows that the real symmetric regularization matrix $\mathbf{\Sigma}^D$ is semi-positive definite [33]. Since the (semi-positive definite) matrix $\boldsymbol{J}^H_k \boldsymbol{J}_k$ in (8) can be very ill-conditioned, a strictly positive definite regularization matrix is needed to enhance convergence. For permittivity vectors $\boldsymbol{\varepsilon}$ with $|\eta| \leq T_{hr}$ for all cells, it follows from Table 1 that $F^D(\boldsymbol{\varepsilon})$ is composed of quadratic or Le Clerc functions only and hence has one single minimum (i.e. $F^D(\boldsymbol{\varepsilon}) = 0$ when $\varepsilon_\nu = \varepsilon_b$ for all ν), such that $\mathbf{\Sigma}^D$ cannot be singular in that part of the domain. Also outside this region strictly positive definiteness can be guaranteed by augmenting the RHS of (25) with a (small) positive number δ

$$\Sigma^D_{\nu,\nu} = \sum_{\nu' \in N_\nu} \sigma_{\nu'} + \delta \tag{27}$$

For the objects considered further in this paper, we did not encounter singularity with WCDA regularization when putting $\delta = 0$. Reconstructions with δ ranging from 10^{-6} to 10^{-2} also gave good results. Note that it follows from Table 1 and the 26 neighborhood system that 26 is the maximum possible value for (25).

Fig. 3 illustrates the quadratic function, LP model, g_h, g_{l-h} and g_{l-c} in the complex domain $\eta = \alpha + j\beta$, together with the corresponding $|\omega|$ and σ functions. Note that $|\omega|$, which is an indication of the smoothing strength, increases monotonically with $|\eta|$ within the 'smoothing' interval (up to a threshold). Outside this interval, $|\omega_{l-c}|$ decreases with increasing $|\eta|$ and becomes zero as $|\eta| \to \infty$. In other words, condition (a) with $C = 0$ entirely prohibits smoothing at discontinuities where $|\eta| \to \infty$, producing sharp edges. g_h and g_{l-h}, with $C > 0$ allow limited (bounded) smoothing—observe that $|\omega_h|$ and $|\omega_{l-h}|$ do not become zero when $|\eta| \to \infty$. However, σ_{l-h} has a steeper slope around zero than σ_h does. The function σ, which is positive around the origin, small for large $|\eta|$ and approaching 0 as $|\eta|$ goes to ∞, performs the role of interaction between two neighbours ε_ν and $\varepsilon_{\nu'}$.

4.2. Numerical analysis

We evaluate the behavior of different WCDA functions in extremely underdetermined situations, which means using far less (simulated) measurements to reconstruct profiles

‡ Note that the strict inequality holds when the cell ν is located next to the boundary of the reconstruction domain $\mathcal{D}$. Expression (25) then also includes terms in $\varepsilon_\nu - \varepsilon_{\nu'}$ for background cells ν' just outside $\mathcal{D}$, but these cells are not included in (26).

		$\lvert\varepsilon_\nu - \varepsilon_{\nu'}\rvert \le T_{hr}$	otherwise
$g_h(\eta)$	$\omega_{\nu'}$	$(\varepsilon_\nu - \varepsilon_{\nu'})$	$\frac{\gamma(\varepsilon_\nu - \varepsilon_{\nu'})}{\lvert\varepsilon_\nu - \varepsilon_{\nu'}\rvert}$
$T_{hr}{=}\gamma$	$\sigma_{\nu'}$	1	$\frac{\gamma}{2\lvert\varepsilon_\nu - \varepsilon_{\nu'}\rvert}$
	$\Sigma^D_{\nu,\nu'}$	-1	$-\frac{\gamma}{2\lvert\varepsilon_\nu - \varepsilon_{\nu'}\rvert}$
$g_{l-h}(\eta)$	$\omega_{\nu'}$	$(\varepsilon_\nu - \varepsilon_{\nu'})e^{-\frac{\lvert\varepsilon_\nu - \varepsilon_{\nu'}\rvert^2}{\gamma}}$	$\gamma\frac{(\varepsilon_\nu - \varepsilon_{\nu'})}{\lvert\varepsilon_\nu - \varepsilon_{\nu'}\rvert}$
$T_{hr}{=}\sqrt{\frac{\gamma}{2}}$	$\sigma_{\nu'}$	$(1 - \frac{\lvert\varepsilon_\nu - \varepsilon_{\nu'}\rvert^2}{\gamma})e^{-\frac{\lvert\varepsilon_\nu - \varepsilon_{\nu'}\rvert^2}{\gamma}}$	$\frac{\gamma}{2\lvert\varepsilon_\nu - \varepsilon_{\nu'}\rvert}$
	$\Sigma^D_{\nu,\nu'}$	$-(1 - \frac{\lvert\varepsilon_\nu - \varepsilon_{\nu'}\rvert^2}{\gamma})e^{-\frac{\lvert\varepsilon_\nu - \varepsilon_{\nu'}\rvert^2}{\gamma}}$	$-\frac{\gamma}{2\lvert\varepsilon_\nu - \varepsilon_{\nu'}\rvert}$
$g_{l-c}(\eta)$	$\omega_{\nu'}$	$(\varepsilon_\nu - \varepsilon_{\nu'})e^{-\frac{\lvert\varepsilon_\nu - \varepsilon_{\nu'}\rvert^2}{\gamma}}$	$\frac{\gamma(\varepsilon_\nu - \varepsilon_{\nu'})}{\gamma + \lvert\varepsilon_\nu - \varepsilon_{\nu'}\rvert^2}$
$T_{hr}{=}\sqrt{\frac{\gamma}{2}}$	$\sigma_{\nu'}$	$(1 - \frac{\lvert\varepsilon_\nu - \varepsilon_{\nu'}\rvert^2}{\gamma})e^{-\frac{\lvert\varepsilon_\nu - \varepsilon_{\nu'}\rvert^2}{\gamma}}$	$\frac{\gamma^2}{(\gamma + \lvert\varepsilon_\nu - \varepsilon_{\nu'}\rvert^2)^2}$
	$\Sigma^D_{\nu,\nu'}$	$-(1 - \frac{\lvert\varepsilon_\nu - \varepsilon_{\nu'}\rvert^2}{\gamma})e^{-\frac{\lvert\varepsilon_\nu - \varepsilon_{\nu'}\rvert^2}{\gamma}}$	$-\frac{\gamma^2}{(\gamma + \lvert\varepsilon_\nu - \varepsilon_{\nu'}\rvert^2)^2}$

Table 1. $\omega_{\nu'}$, $\sigma_{\nu'}$ and $\Sigma^D_{\nu,\nu'}$ for the three proposed WCDA functions.

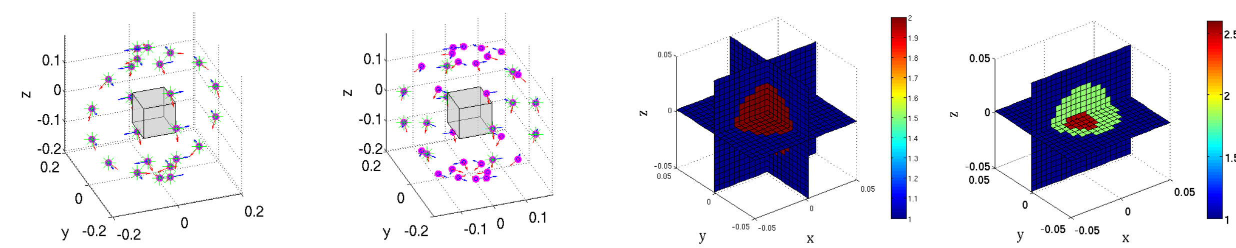

(a) Configuration C1 (b) Configuration C2 (c) Object A (d) Object B

Figure 4. Antenna configurations and objects used in the numerical analysis. Only real parts of the complex permittivity are shown in (c) and (d).

with a large number of permittivity unknowns. More particularly, we will observe the influence of the parameter γ in the models g_h, g_{l-c} and g_{l-h} on the reconstructions, which will help us to select a suitable value for this parameter, when dealing with

- Objects of different complexity: We consider piecewise homogeneous objects with dimensions of the order of a (few) wavelength(s) (at 8 GHz, $\lambda_0 = 3.75$ cm). Object

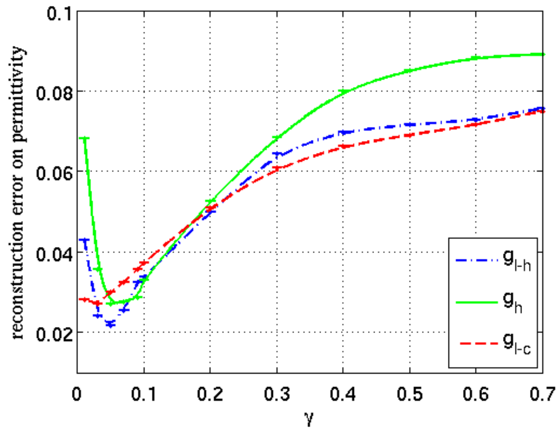

(a) Object A with Configuration C1

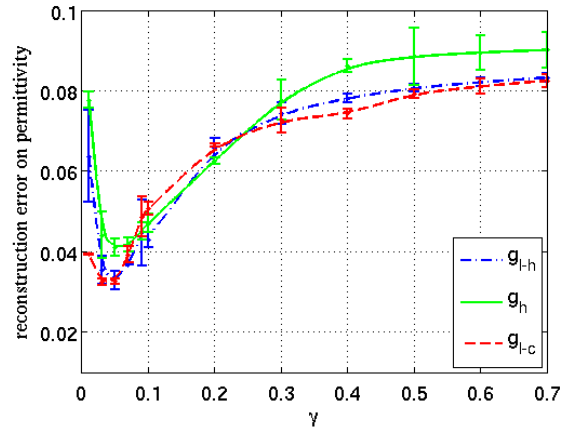

(b) object B with Configuration C1

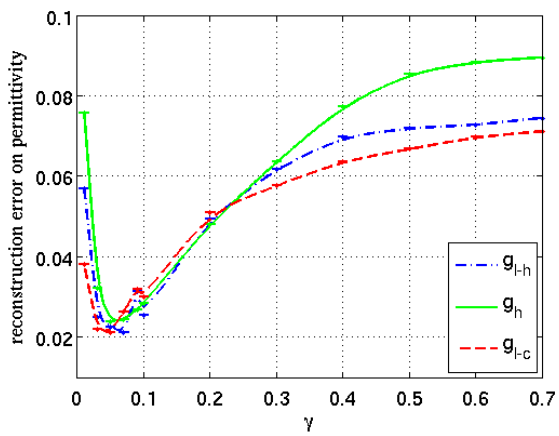

(c) Object A with configuration C2

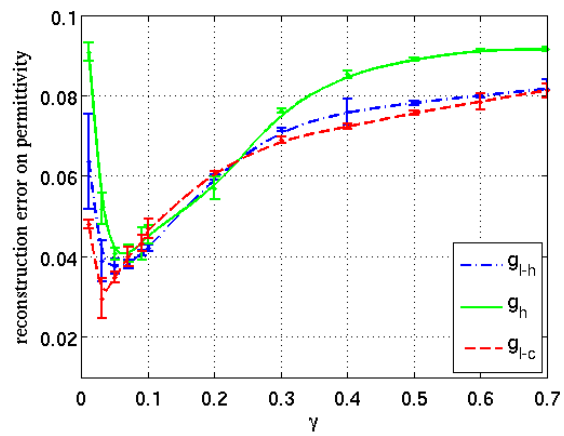

(d) object B with configuration C2

Figure 5. Reconstruction error as a function of γ for the WCDA models g_h, g_{l-c} and g_{l-h} ($\mu = 8 \times 10^{-7}$). Simulations are shown for the objects and antenna configurations from Fig.4 at SNR = 30 dB.

A (Fig. 4 (c)) is a homogeneous sphere with radius 3 cm (diameter = $1.6\lambda_0$) and permittivity 2; object B (Fig. 4 (d)) is a small sphere with radius 1.5 cm and permittivity $2.5 - j$ in a big sphere with radius 3 cm and permittivity 1.8; the side of the reconstruction domain $\mathcal{D}$ is 10 cm ($2.7\lambda_0$) and the number of unknown permittivity cells is 8000.

- Different sparse antenna configurations: Configuration C1 (Fig. 4 (a)) consists of 24 antenna positions (4 meridians with 6 evenly spaced positions each) with 48 transmitting dipoles (2 polarizations per position) and 48 receiving dipoles (same locations and polarizations), resulting in 2304 complex data. Configuration C2 (Fig. 4 (b)) consists of 36 antenna positions (6 meridians with 6 positions each) with less (24) transmitting dipoles (only the 12 positions on the 2 parallels closest to $z = 0$ are used, again with both polarizations) and more (72) receiving dipoles, yielding 1728 complex data. The actual numbers of non-redundant data are even

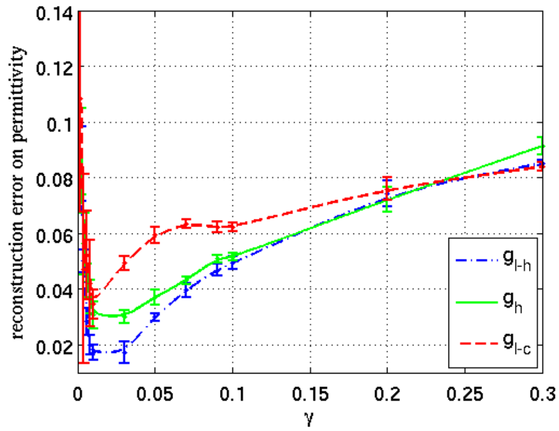

(a) Object A with Configuration C1

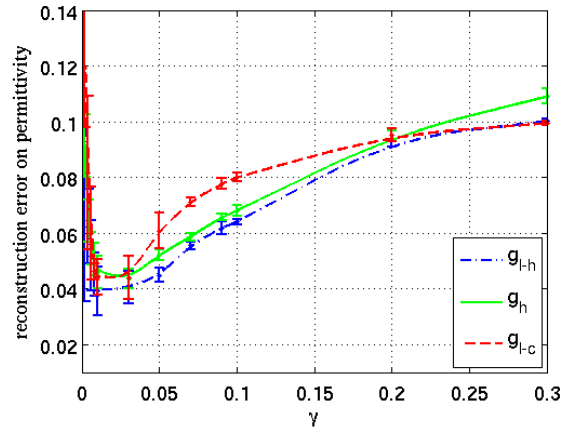

(b) object B with Configuration C1

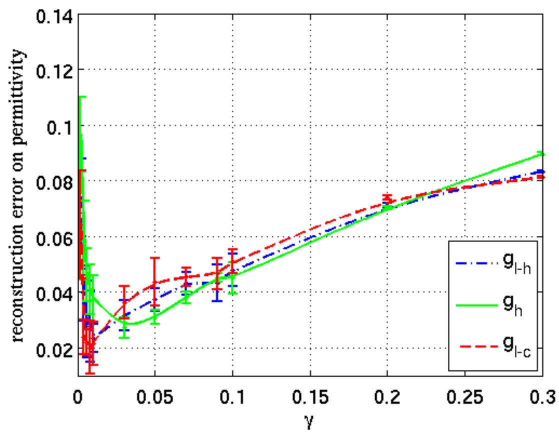

(c) Object A with configuration C2

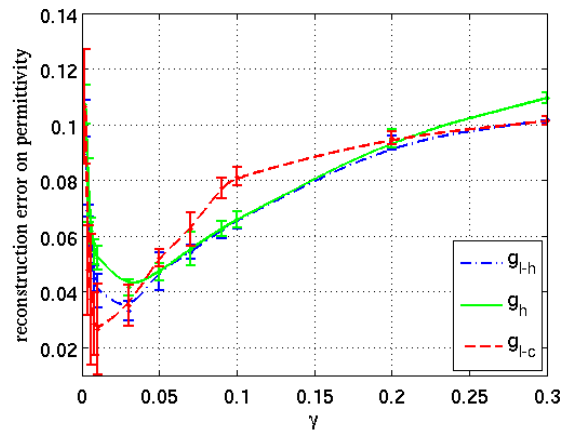

(d) object B with configuration C2

Figure 6. Reconstruction error as a function of γ for the WCDA models g_h, g_{l-c} and g_{l-h} ($\mu = 8 \times 10^{-6}$). Simulations are shown for the objects and antenna configurations from Fig.4 at SNR = 25 dB.

lower due to reciprocity.

- Different levels of noise: We experiment with different levels of additive white Gaussian noise resulting in signal-to-noise ratios (SNR) from 20 dB to 30 dB (i.e. typical SNRs in a microwave imaging experiment).

We refer to Section 5 for the definition of several other reconstruction parameters. To evaluate the quality of the permittivity reconstructions, the reconstruction error R is defined as

$$R = \frac{1}{\|\boldsymbol{\varepsilon}^{ref}\|} \parallel \boldsymbol{\varepsilon}^{rec} - \boldsymbol{\varepsilon}^{ref} \parallel \tag{28}$$

which expresses the normalized difference between the reference $\boldsymbol{\varepsilon}^{ref}$ and reconstructed $\boldsymbol{\varepsilon}^{rec}$ permittivity values on the grid. We set the initial guess $\boldsymbol{\varepsilon}_{init} = [1, \cdots, 1]$. We verified that other (reasonable) choices of this initial estimate did not influence much the final reconstruction error.

Figs. 5 and 6 show the reconstruction error for the three WCDA models applied to the objects and antenna configurations from Fig.4, as a function of the parameter γ at SNR = 30 dB ($\mu = 8 \times 10^{-7}$) and SNR = 25 dB ($\mu = 8 \times 10^{-6}$), respectively. We ran each experiment (situation) 10 times and plot the average values of the reconstruction errors at distinct values of γ of each model in each subfigure of Fig. 5 and 6. Error bars indicate the absolute deviation of reconstruction errors. The following observations can be made: (i) From the reconstruction error point of view, it is difficult to say which model is the best. g_{l-h} yields the smallest error with Object A in Configuration C1 while g_{l-c} yields the smallest error with Object B in Configuration C2; (ii) From the visual reconstruction quality point of view (smooth surface and sharp edges), g_{l-c} always produces better uniform values for different materials and sharper edges than g_{l-h} and g_h. Take Object A and Configuration C1 (Fig. 5 (a)) at SNR = 30 dB as an example, and adopt γ that (approximately) yields the smallest reconstruction error–we define such γ as "optimal" in the following—with each model ($\gamma = 0.04$ for g_{l-h}, $\gamma = 0.06$ for g_h and $\gamma = 0.03$ for g_{l-c}). Fig. 7 shows the corresponding reconstructions. We can see from this example that both g_{l-h} and g_h produce some artifacts, but not g_{l-c}. Although g_{l-c} results in a bigger error (0.0301) than the other two models (0.026 and 0.0292), the reconstruction of g_{l-c} appears better visually (free of artifacts); (iii) From the error curve trend of view, the Huber function g_h is the most stable for different targets and antenna configurations (only one minimum for a certain level of noise). The functions g_{l-h} and g_h behave similarly for SNR = 30 dB and SNR = 25 dB. The curves of g_{l-c} seem unstable for the higher noise level. The reason for these large fluctuations is in the fact that g_{l-c} tends to keep sharp edges, which can erode or dilate the objects. The optimal value of γ for g_{l-c} is smaller than that for g_{l-h} at the same noise level.

Observe that the reconstruction errors under Configuration C2 most often are (slightly) smaller than those under Configuration C1, for each of the objects. Configuration C2 with more receiving positions apparently performs best. We also notice that g_{l-h} and g_h yield mostly a smaller reconstruction error than g_{l-c} under Configuration C1 but a larger error than g_{l-c} under Configuration C2; With the same configuration, more complicated objects produce larger errors than simple ones; With free space background and simulated data, the error curves have similar general trends for different targets and antenna configurations at a specific noise level.

The analysis above agrees with the properties of the WCDA models illustrated in Fig. 3. A model with a sharply peaked σ (i.e. highly sensitive AIF) and a $|\omega|$ with $C > 0$ (bounded smoothing) has the potential to yield smaller reconstruction errors. That is why the error for g_{l-h} is most of the time smaller than for g_{l-c} in the high SNR case. Of course when the value of γ is decreased, σ_h will approach σ_{l-h}. Models with $C = 0$, as g_{l-c} and g_s [21], can produce sharp edges but can also erode or dilate the surface of original objects. So depending on the application of microwave imaging, one can choose different models from this WCDA class.

In order to show that a suitable value of γ is not much influenced by variations in the (electrical) size of the object and of $\mathcal{D}$, we also conducted a few simulations for a

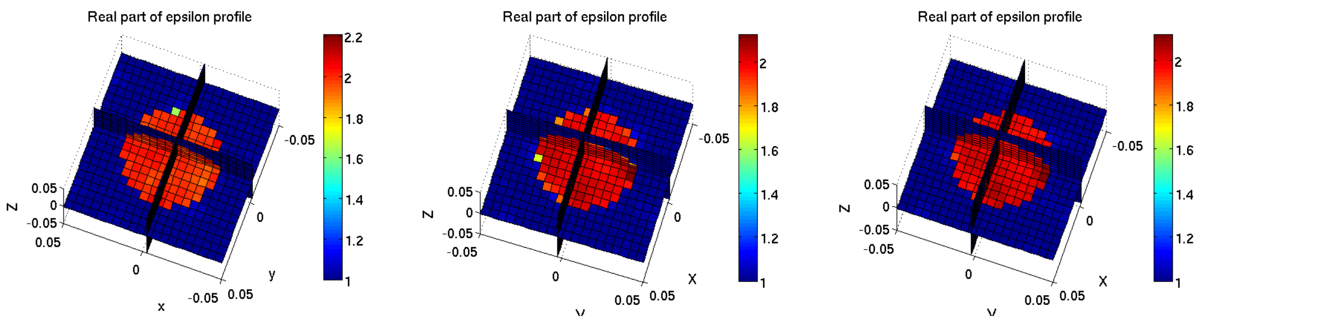

(a) g_{l-h}, $\gamma = 0.04$ (error=0.0260)

(b) g_h, $\gamma = 0.06$ (error=0.0292)

(c) g_{l-c}, $\gamma = 0.03$ (error=0.0301)

Figure 7. Reconstructions with smallest reconstruction error obtained with each model for object A and antenna configuration C1 at SNR = 30 dB ($\mu = 8 \times 10^{-7}$).

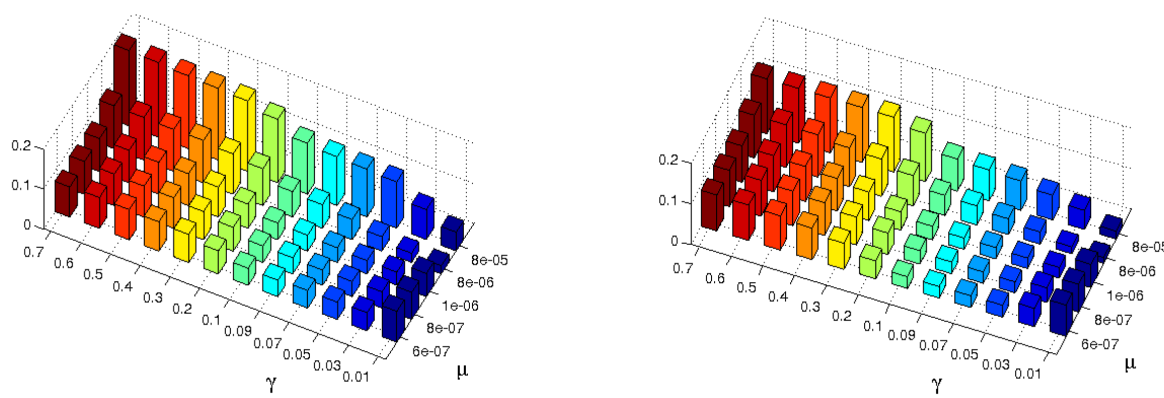

Figure 8. Reconstruction error R as a function of μ and γ at SNR = 30 dB. Left: for g_{l-h}, object B and antenna configuration C2; Right: for g_h, object A and antenna configuration C1.

larger homogeneous object C (as object A but with radius 6.0 cm or diameter $= 3.2\lambda_0$) in $\mathcal{D}$ with side 15 cm ($= 4\lambda_0$) and for a larger inhomogeneous object D (a small sphere with radius 1.5 cm (permittivity 2.5) inside a sphere with radius 3 cm (permittivity 1.8) embedded in a sphere with radius 5 cm and permittivity 1.5) in $\mathcal{D}$ with side 10 cm. The number of transmitting positions was increased to 36 resulting in 5184 data. The optimal values for γ are 0.06 for object C and 0.04 for object D at a SNR of 30 dB ($\mu = 8 \times 10^{-7}$) and hence in the same range as the optimal values for the objects in Fig. 5.

The regularization parameter μ in (5) is approximately optimized by means of numerical simulations, similarly as with the parameter γ, but with averaging over 3 experiments. Fig. 8 shows the reconstruction error in the $\mu - \gamma$ plane for 2 different configurations at 30 dB, from where we notice that the minimum is around $\mu = 10^{-5}$ and $\gamma = 0.01$. It can be seen that moving too far away from these optimal values leads to a significant increase in the reconstruction error. Note that the lower value of μ

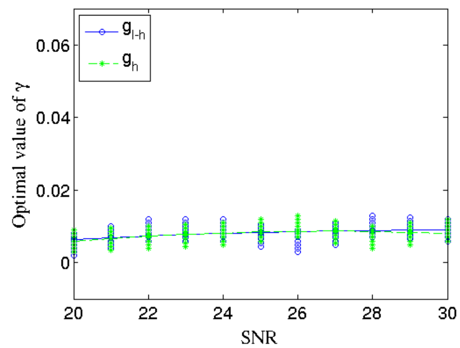

Figure 9. Optimal values of γ (yielding approximately the smallest reconstruction errors) as a function of the SNR for g_{l-h} and g_h and for object B and antenna configuration C1. Here $\mu = 8 \times 10^{-5}$ for 20 dB $<$ SNR $<$ 25 dB and $\mu = 10^{-5}$ for 25 dB $\leq$ SNR $<$ 30 dB.

($\mu = 8 \times 10^{-7}$) used in Fig. 5 together with the corresponding optimal values for γ thus lead to somewhat higher reconstruction errors in Fig. 7. We observed that at 20 dB the minimum is about $\mu = 8 \times 10^{-5}$ and $\gamma = 0.01$. We conclude that the optimal regularization parameter μ appears to be sensitive to the SNR, while the optimal γ remains quasi invariant and equal to approximately 0.01 for all three WCDA functions, when applying different SNR, see also Fig. 9, or when employing different objects and antenna configurations that conform with the specifications at the beginning of this subsection.

5. Numerical data validation

We performed reconstructions from simulated data with three different antenna configurations, including a configuration similar to [16], shown in Fig. 10 (a) and two much sparser configurations shown in Fig. 10 (b) and Fig. 10 (c). The sparse configurations are attractive in terms of computation time but are challenging due to the highly underdetermined situation. We compare the reconstruction results for the WCDA models (g_h, g_{l-h} and g_{l-c}) with two other regularizations: multiplicative smoothing (MS) [10] and step-wise relaxed value picking (SRVP) [16].

The frequency is 8 GHz ($\lambda_0 = 3.75$ cm). The scattering object corresponds to object B from Section 4 and is positioned in the center of $\mathcal{D}$, which is a cube of edge length 10 cm centered in a reference frame (see Fig. 10). The big and small spheres are centered at the origin (0,0,0) and at the point (-0.56 cm, -0.56 cm, -0.56 cm), respectively (see Fig. 11(a)). The reconstruction domain is discretized in $20 \times 20 \times 20$ voxels with edge size 5 mm ($0.13\lambda_0$), yielding a total of 8000 permittivity unknowns. We use this grid for both forward and update problems as well as for generating the simulated scattered field data. This way the reconstruction is not bothered by discretization noise and it can be exact in absence of (simulated) measurement noise on the scattered field data. Our testing of the proposed regularizations thus is affected only by this measurement

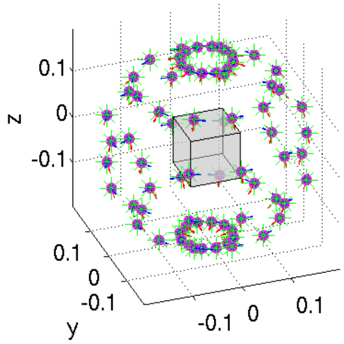

(a) 20736 data

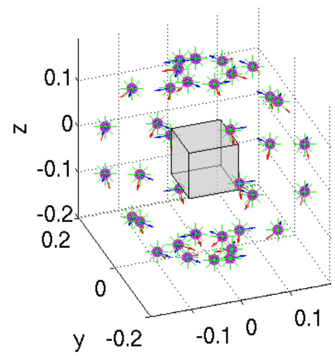

(b) 5184 data

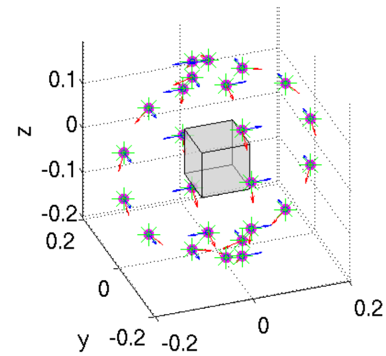

(c) 2304 data

Figure 10. Three configurations with antenna positions (dots) on a sphere with radius 20 cm. The arrows in two orthogonal directions indicate transmitting dipoles. The cube in the center indicates the reconstruction domain $\mathcal{D}$.

noise. We set additive white Gaussian noise with a SNR of 30 dB. The tolerance for the BICGSTAB iterative routine is set to 10^{-3}.

The elementary dipoles in Fig. 10 are evenly distributed over a number of meridians with radius 20 cm. Their positions and orientations are indicated with dots and arrows, respectively. For every transmitter position, dipole orientations along $\hat{\boldsymbol{u}}_\theta$ and $\hat{\boldsymbol{u}}_\phi$ are used and the scattered field is measured in every position along these directions. The configuration in Fig. 10 (a) consists of 144 dipoles (12 meridians with 6 positions each) which generate 20736 complex data numbers; the sparser configuration in Fig. 10 (b) consists of 72 dipoles (6 meridians with 6 positions each), generating 5184 complex data; the sparsest configuration in Fig. 10 (c) consists of 48 dipoles (4 meridians with 6 positions each) which generate 2304 complex data. So the length of the data vector $\mathbf{e}^{meas}$ ranges from $N^d = 2304$ to 20736; taking into account reciprocity, the number of non-redundant data is actually $N^d/2$. Referring to the estimate M [27] of the NDF in each component of a (single-view) 3D radiated field, it follows that $M = 25$ to $M = 32$ for object B at 8 GHz; the corresponding information is accessible by uniformly positioning M receivers over the measurement sphere. Let us indicatively compare the configurations of Fig. 10—the antenna positioning is not uniform there—to this NDF estimate: with configuration (a) the number of positions (72) largely exceeds the NDF; with sparse configuration (b) the number of positions (36) is of the order of the NDF, while the sparsest configuration (c) counts a lower number of positions (24) than the NDF §.

The initial estimate of the permittivity in $\mathcal{D}$ is chosen equal to the background permittivity. We set $\gamma = 0.01$ for the three WCDA potential functions and the regularization parameter $\mu = 10^{-5}$. We choose $\mu = 10^{-4}$ for MS [10] and $\mu = 0.1$ for SRVP [16] ($\mu = 2$ for sparsest data from Fig. 10 (c)).

§ Note that the NDF criterion is valid only if the distance between the object and the antennas is at least a few wavelengths [27], while our reconstruction algorithm is not restricted to such configurations.

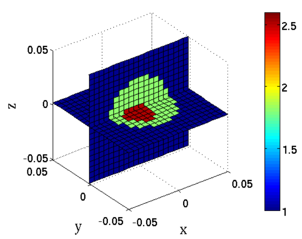

(a) reference (b) MS, R=7.83% (c) SRVP, R=4.49%

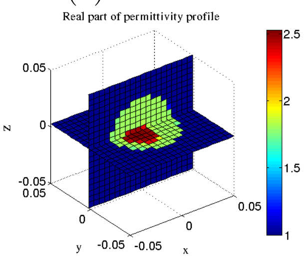

(d) g_h, R=1.29% (e) g_{l-h}, R=0.66% (f) g_{l-c}, R=1.18%

Figure 11. Real part of the complex permittivity profile for the antenna configuration from Fig. 10 (b). (a) reference and reconstructions for (b) MS; (c) SRVP; (d) g_h; (e) g_{l-h}; (f) g_{l-c}.

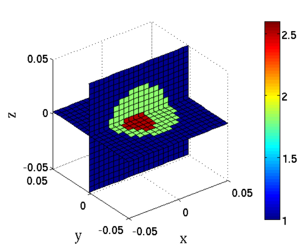

(a) reference (b) MS, R=8.84% (c) SRVP, R=14.60%

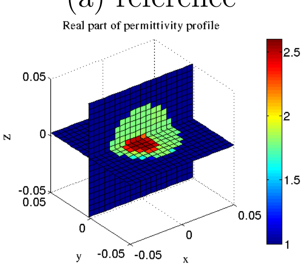

(d) g_h, R=2.69% (e) g_{l-h}, R=1.85% (f) g_{l-c}, R=3.90%

Figure 12. Real part of the complex permittivity profile for the antenna configuration from Fig. 10 (c). (a) reference and reconstructions for (b) MS; (c) SRVP; (d) g_h; (e) g_{l-h}; (f) g_{l-c}.

Reconstruction error	MS	SRVP	g_h	g_{l-h}	g_{l-c}
20736 complex data	6.84%	2.61%	0.66%	0.36%	0.65%
5184 complex data	7.83%	4.49%	1.29%	0.66%	1.18%
2304 complex data	8.84%	14.60%	2.69%	1.85%	3.90%

Table 2. Reconstruction error for the different regularization functions and antenna configurations from Fig. 10.

The computation time is similar for all three considered regularizations provided that equal numbers of antennas are employed. The chosen antenna configuration has a large impact on the reconstruction time: the sparsest configuration Fig. 10 (c) requires only around 30 minutes while around 2 hours were needed for configuration Fig. 10 (a), using the same stopping criterion $F^{LS} = 10^{-3}$ or 20 iterations maximum, on a six-core Intel i7 980x processor (3.33GHz) with 24GByte memory. Further speed-up would be possible by applying multi-threading or by parallel processing, e.g. [34].

The reconstruction error (28) is shown in Table 2 for the three antenna configurations. Reconstructed images are shown in Figs. 11 - 12. Table 2 shows that the proposed WCDA models yield smaller reconstruction errors for all antenna configurations: the error reduction is significant with respect to MS in all experiments and with respect to SRVP in the sparse configurations. Figs. 11 - 12 show that the reconstructions of MS are over-smoothed as expected. SRVP retains sharp edges but deteriorates drastically when the data is decreasing. The reconstructions from WCDA are much closer to the exact profile. These images illustrate the improvement visually and demonstrate the potential of the proposed method for reconstruction from sparse measurements.

6. Reconstructions from real measurements

Now we perform reconstructions from real measurements for 3D targets from the Fresnel database [23]. These carefully measured experimental data have been inverted with various methods by several authors, see e.g. the special section [24]. This enables comparing the potential of WCDA regularization against a number of other regularization strategies that were used for the inversion of the same objects. We select single frequency data from the available multiple frequency data. As in the previous section we also extract sparse data subsets and for each data set we compare reconstructions with MS regularization and WCDA regularization with the three potential functions g_{l-h}, g_{l-c} and g_h. We consider four quasi-lossless dielectric targets: TwoSpheres, TwoCubes, CubeSpheres and Myster. They are shortly described in the following subsections, but we refer to [23] for more details.

In the experimental setup the target is placed in the center of a reference frame and illuminated with plane waves radiated by a parabolic antenna, which is moved on a sphere with radius $R = 1.796$ m. The receiving antenna is moved in the horizontal plane

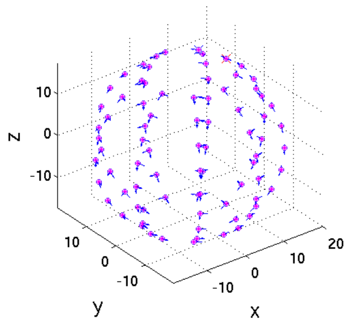

(a) 81 transmitters

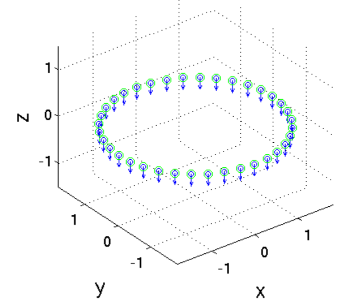

(b) 36 receivers

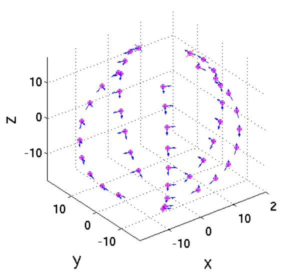

(a1) 45 transmitters

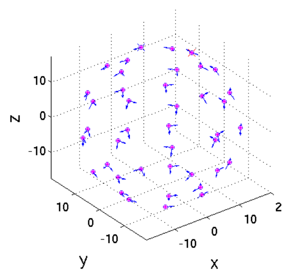

(a2) 41 transmitters

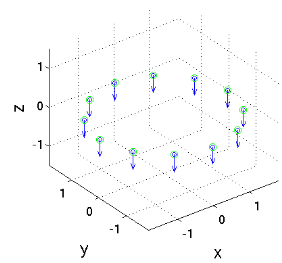

(b1) 12 receivers

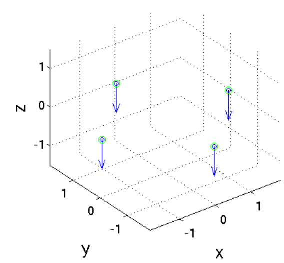

(b2) 4 receivers

Figure 13. The dipole configurations in the forward model: 81 transmitting positions or 162 transmitting dipoles (oriented along the θ and ϕ directions) are placed on a sphere with radius 20 m (a) and 36 receiver positions are placed on a circle with radius 1.796 m in the horizontal plane (b). Subsampled configurations: (a1) 45 transmitting positions (90 dipoles); (a2) 41 transmitting positions (82 dipoles); (b1) 12 receiver positions; (b2) 4 receiver positions.

on a circle with the same radius. We refer to [23] for further details on the setup and the measurements. In our forward model transmitting elementary dipoles are positioned on a sphere with radius $R = 20$ m — to simulate an incident plane wave at the target location [15] — and for each position oriented along the polar $\hat{\boldsymbol{u}}_\theta$ and azimuthal $\hat{\boldsymbol{u}}_\phi$ directions; the receiving dipoles are equally spaced on a circle with radius $R = 1.796$ m in the horizontal plane and oriented along the negative z axis. In a full data set (Fig. 13 (a)), there are 81 transmitting positions (θ_T, ϕ_T) with ϕ_T varying from 20° to 340° by steps of 40° (i.e. 9 meridians) and θ_T from 30° to 150° by steps of 15° (i.e. 9 parallels), which yields 162 illuminations in total; there are 36 receivers positioned from 0° to 350° (10° spacing), see Fig. 13 (b); due to technical limitations not all source-receiver combinations can effectively be used, including the receivers that are closer to the source meridian than 50°, which results in a data vector with maximum dimension of $N^d = 4374$ for a full single frequency data set. Note that all contributions in [24], which we will use for comparison in this section, used full single or multiple frequency data sets.

In this section we use downsampled data sets derived from a full data set. Let us consider two different subsampling strategies for the transmitters: a spread along a subset of 5 meridians (Fig. 13 (a1)) and a rather uniform spread (Fig. 13 (a2)); and

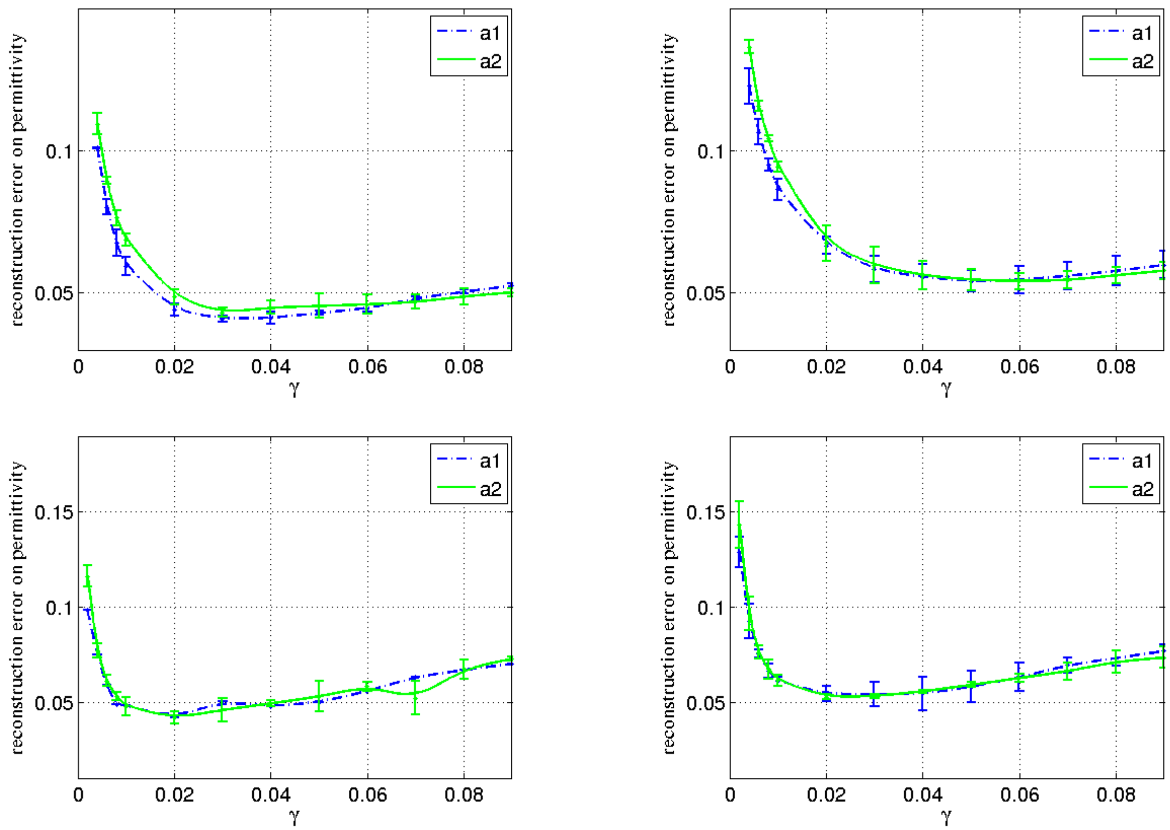

Figure 14. Reconstruction error as a function of γ for two subsampling strategies (a1)(b1) and (a2)(b1). Object A (left) and object B (right) from Fig. 4 at SNR = 30 dB (top) and SNR = 25 dB (bottom).

two subsets for the receivers: 12 receivers with $\phi_R = 0°$ to $\phi_R = 330°$ (30° spacing) in Fig. 13 (b1) and 4 receivers with $\phi_R = 0°$ to $\phi_R = 270°$ (90° spacing) in Fig. 13 (b2). Due to the aforementioned technical limitations only 9 respectively 3 of these receivers are effectively employed. Transmitter configuration (a1) has 45 transmitting positions (θ_T, ϕ_T) with ϕ_T varying from $\phi_T = 20°$ to $\phi_T = 340°$ by steps of 80° and with $\theta_T = 30°$ to $\theta_T = 150°$ by steps of 15°, yielding 90 illuminations and configuration (a2) has 41 transmitting positions (θ_T, ϕ_T) resulting from the intersection of $\theta_T = (30°, 60°, 90°, 120°, 150°)$ with $\phi_T = (20°, 100°, 180°, 260°, 340°)$ and the intersection of $\theta_T = (45°, 75°, 105°, 135°)$ with $\phi_T = (60°, 140°, 220°, 300°)$ yielding 82 illuminations. The number of data for these down-sampled sets range from approximately $N^d = 243$ for the sparsest configuration (a2)(b2) to $N^d = 810$ for (a1)(b1). Reconstructions with the sparsest data sets take around 30 minutes while 3 hours are needed with the full data sets, using the same stopping criterion $F^{LS} = 10^{-3}$ or 20 iterations maximum, on a six-core Intel i7 980x processor (3.33GHz) with 24 GByte memory (multi-threading was not applied here).

To test the difference between the two transmitter downsampling strategies (a1) and (a2), we first conducted reconstructions from simulated data perturbed with noise using the same objects as in Fig. 4 (c) (d) and the antenna configurations (a1) (b1) (808 data) and (a2) (b1) (736 data) from Fig. 13. The reconstruction error for WCDA g_{l-h} is shown in Fig. 14 at SNR 30 dB (top) and 25 dB (bottom). We observe that the configuration (a2) with approximately uniformly spread antennas on the sphere yields similar reconstruction errors than the meridian-based configuration (a1), even though more antennas were employed in configuration (a1). Thus we will use the uniform subsampling (a2) in the following of this section.

As in [15] we choose the highest available frequency $f = 8$ GHz ($\lambda_0 = 3.75$ cm) to reconstruct the TwoCubes, CubeSpheres and Myster targets, which combines a sufficient resolution and a good convergence of the algorithm. For the larger TwoSpheres target we adopt $f = 4$ GHz ($\lambda_0 = 7.50$ cm), such that all targets have approximately the same electrical size. A calibration is applied to match amplitude and phase between measured and simulated fields: for each incidence, the measured scattered field values are multiplied with a complex factor, which is the ratio of the simulated and the measured incident fields at the receiver located opposite to the source.

All reconstructions start from the domain filled with air as an initial estimate of the permittivity. We use the same discretization for both the forward and inverse grids. Only the real parts of the permittivities are shown, since the imaginary parts are negligible. Since we assume that SNR = 20 dB for the Fresnel data [15], we set $\gamma = 0.008$ and $\mu = 10^{-4}$ for the WCDA models; we take $\mu = 10^{-3}$ for MS [15].

6.1. TwoSpheres

This target consists of two spheres with diameter 5 cm ($= 0.67\lambda$ at 4 GHz) and permittivity 2.6. They are centered at (-2.5 cm, 0, 0) and (2.5 cm, 0, 0). We subsampled the data according to the antenna configurations (a2) (b2) from Fig. 13, yielding a data vector with dimension $N^d = 243$. The reconstruction domain $\mathcal{D}$ is a 16 cm $\times$ 8 cm $\times$ 8 cm box and is discretized in $40 \times 20 \times 20$ cells with a cell size of 4 mm ($0.053\lambda_0$), yielding a total of 16000 permittivity unknowns. The problem thus is heavily underdetermined.

Fig. 15 shows the reconstructions with the different methods for this object. The reconstruction with MS in Fig. 15 (a) strongly smoothed the edges, which makes it difficult to estimate the permittivity and diameter of the spheres. Figs. 15 (b)-(d) with WCDA instead show much sharper edges and a better homogeneity. Edges are smoother with g_h than with g_{l-h} and g_{l-c} and g_h also shows slightly larger permittivity fluctuations inside the spheres. Furthermore, g_{l-c} yields the sharpest edges of all reconstructions; a xz cross-sectional view is shown in Fig. 16: the spheres are a bit oversized and their average permittivity is 2.5, which is close to the expected value.

By comparing visually the results in Figs. 15 and 16 to reconstructions of the same target by some of the methods in [24], we can conclude that WCDA often yields better results from significantly fewer measurements. Smoothed edges were reconstructed in Fig. 3 of [35] from a full single-frequency dataset at the same frequency $f = 4$ GHz with Tikhonov regularization. Sharp edges and permittivity values of about 2.6 were

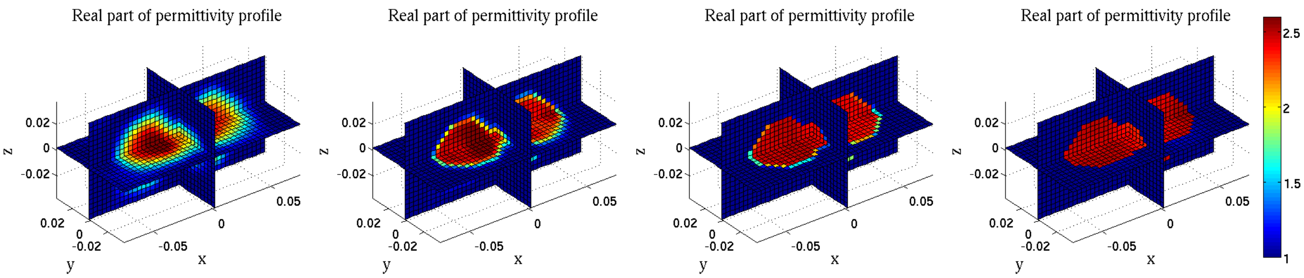

(a) MS (b) g_h (c) g_{l-h} (d) g_{l-c}

Figure 15. Real part of the complex permittivity for the *TwoSpheres* target. Reconstructions (using 243 data) from the sparsest antenna configuration (a2) (b2) of Fig. 13 at 4 GHz with: (a) MS, (b) g_h, (c) g_{l-h} and (d) g_{l-c}.

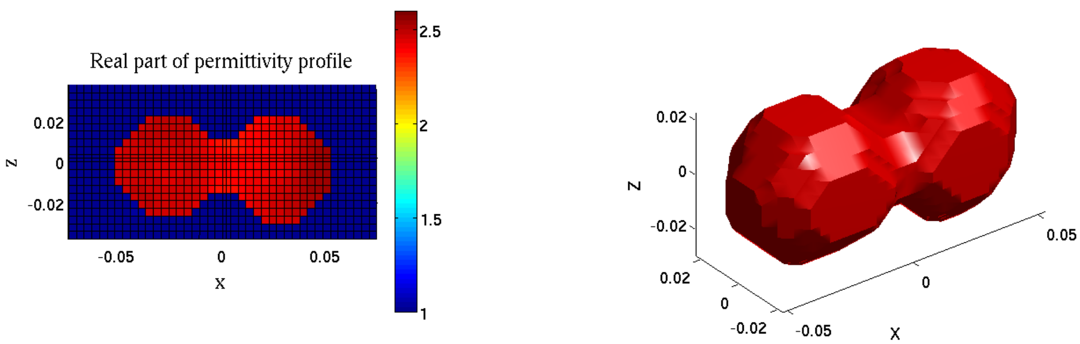

Figure 16. Cross section of g_{l-c} at $y = 0$ (left) and 3D iso-surface of the permittivity (right), corresponding to Fig. 15 (d).

reconstructed using all 21 frequencies with weighted L2 norm - TV regularization in Fig. 3 of [36]. The reconstructions in Fig. 2 (e)-(f) of [15] from a full single-frequency dataset at 4 GHz with SRVP regularization combined with extra *a priori* information also yield an average permittivity of 2.5 but better sized spheres than our results with g_{l-c}.

6.2. *TwoCubes*

This target consists of two cubes with edge length 2.5 cm (= 0.67λ at 8 GHz) and permittivity 2.3. They are centered at (1.25 cm, -1.25cm, 3.75cm) and (-1.25 cm, 1.25 cm, 6.25 cm). We subsampled the data according to the antenna configurations (a2) (b1) from Fig. 13, yielding a data vector with dimension N^d= 736. The reconstruction domain $\mathcal{D}$ now is a 7 cm $\times$ 7 cm $\times$ 7 cm box, centered at (0, 0, 5 cm) and discretized in 25 $\times$ 25 $\times$ 25 cells with a cell size of 2.8 mm ($0.075\lambda_0$), yielding a total of 15625 permittivity unknowns.

The reconstructions are shown in Fig. 17. Similar observations hold as with the TwoSpheres object. The reconstruction with MS in Fig. 17 (a) strongly smoothed the edges. For the reconstructions with WCDA in Figs. 15 (b)-(d), the cubes are

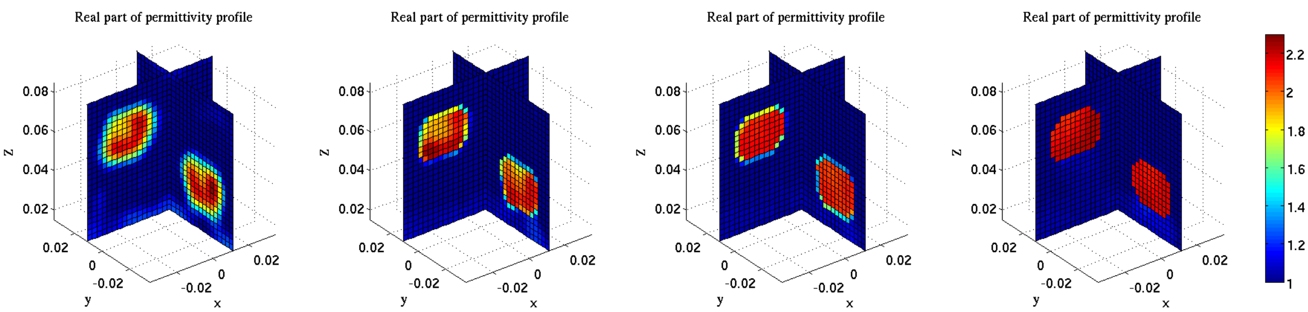

(a) MS (b) g_h (c) g_{l-h} (d) g_{l-c}

Figure 17. Real part of the complex permittivity for the *TwoCubes* target. Reconstructions (using 736 data) from the sparse antenna configuration (a2)(b1) of Fig. 13 at 8 GHz with: (a) MS, (b) g_h, (c) g_{l-h} and (d) g_{l-c}.

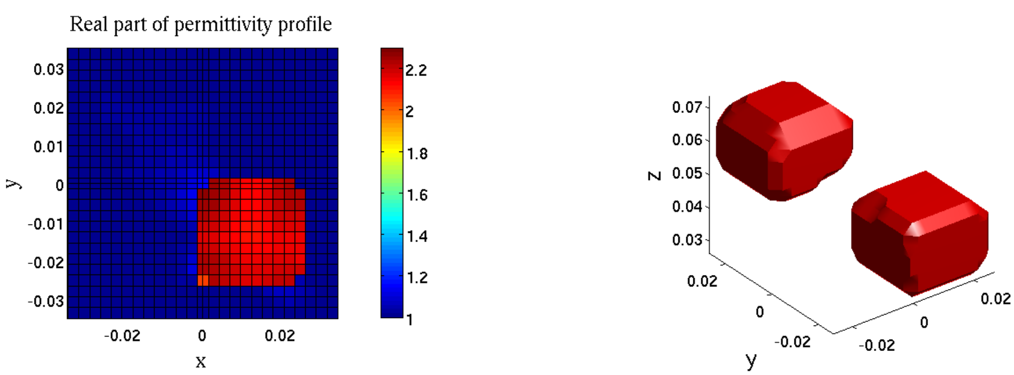

Figure 18. Cross section of g_{l-c} at $z = 5$ cm (left) and 3D iso-surface of the permittivity (right), corresponding to Fig. 17 (d).

reconstructed in the right locations but the edges are a bit eroded and the edge length in the z-direction is a bit too small (this length is improved when using more data). The function g_{l-c} still yields the sharpest edges among all reconstructions; the average permittivity of 2.2 in the cubes is close to the expected value; a xy cross-sectional view and the erosion of the edges are illustrated in Fig. 18.

Edge degradations are observed in all contributions of [24], e.g.: in Fig. 8 of [35] from a full single-frequency dataset at 8 GHz, where Tikhonov regularization was applied and which furthermore shows permittivity fluctuations inside the cubes; in Figs. 4-7 of [37] from a full single-frequency dataset at 5 GHz, where a Bayesian framework was used to account for the experimental noise and which show blurred edges and in Fig. 9 (b) of [38] at 8 GHz, obtained with frequency hopping from filtered data sets which shows quite rounded shapes of the cubes. Figure 6 (c)-(d) in [15] from a full single-frequency dataset at 8 GHz, obtained with SRVP regularization combined with extra *a priori* information, show homogeneous objects with permittivity 2.3 and sharp edges but some erosions can still be seen in Fig. 9.

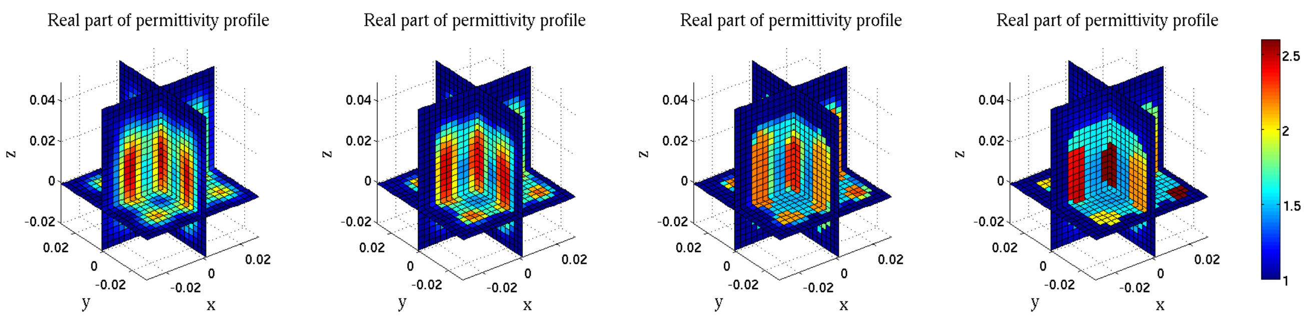

(a) MS (b) g_h (c) g_{l-h} (d) g_{l-c}

Figure 19. Real part of the complex permittivity for the *CubeSpheres* target. Reconstructions (using 736 data) from the sparse antenna configuration (a2) (b1) of Fig. 13 at 8 GHz with: (a) MS, (b) g_h, (c) g_{l-h} and (d) g_{l-c}.

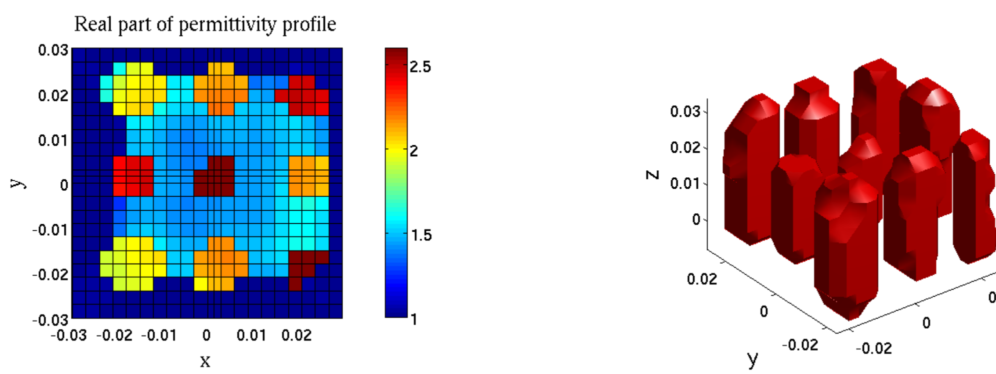

Figure 20. Cross section of g_{l-c} in (d) at $z = 1$ cm (left) and 3D iso-surface of the permittivity (right), corresponding to Fig. 19 (d).

6.3. CubeSpheres

This target is an aggregate of 27 spheres in a $3 \times 3 \times 3$ cubic stacking with edge length 4.76 cm ($= 1.3\lambda$ at 8 GHz). Each sphere has a diameter of 1.59 cm ($= 0.4\lambda$) and a permittivity of 2.6. Due to the size of the spheres and their arrangement, this target has the finest geometrical details. We subsampled the data according to the antenna configurations (a2) (b1) from Fig. 13, yielding a data vector with dimension $N^d = 736$. The reconstruction domain $\mathcal{D}$ is a 6 cm$\times$ 6 cm$\times$ 6.9 cm box, centered at (0, 0, 1.45 cm) and discretized in $20 \times 20 \times 23$ cells with cell size 3 mm, yielding a total of 9200 permittivity unknowns.

Fig. 19 shows the results from the different methods. The 3 by 3 stacking is clearly visible in the horizontal xy-plane but individual spheres are not resolved along the z-direction. This is due to the specific antenna configuration of the database with receiving antennas only in the horizontal plane. With WCDA in Fig. 19 (b)-(d), the edges again are much better reconstructed than with MS in Fig. 19 (a), in particular with g_{l-c}. An xy cross-section is given in Fig. 20. It shows permittivity variations from 2.0 to 2.6 for the spheres; all spheres are undersized, particularly those with the highest permittivities, which is compensated with a higher value for the background permittivity in between the spheres.

In [39], where no additional regularization was applied, the image from a full single-frequency dataset at 8 GHz in Fig. 6 (f) shows several smoothed spheres as well as artifacts in the background. In [35], where Tikhonov regularization was used, the spheres in the xy plane are well distinguished at 8 GHz in Fig. 20, but the edges are not very clear and the shapes suffer from the coarser grid. Even in reconstructions from multi-frequency data in [36], it is difficult to distinguish the individual spheres in the contrast profiles in Fig. 22-23. where the weighted L2 norm TV regularization tends to smooth out the discontinuities; this is somewhat improved with L2 norm TV regularization in Fig. 24 but the permittivity ($\varepsilon \approx 1.7$) is underestimated; the reconstruction shown in Fig. 13 (a) in [38], obtained with frequency hopping and data filtering, shows the individual spheres although smoothed and with a maximum permittivity of about 2.1. With SRVP regularization in [15], Fig. 10 (b) shows rather well sized-spheres with homogeneous permittivity values of about 2.1.

6.4. Myster

This target was a mystery target until the publication of [24]. It is a group of 12 spheres with permittivity 2.6 and diameter 23.8 mm ($= 0.64\lambda$ at 8 GHz), arranged so that their centers lay along the vertices of an icosahedron [23]. It was positioned in the same way as the CubeSpheres target, so that the xoy axis crossed the center of the three spheres on which the mystery target lays. We selected data according to the antenna configurations in Fig 13 (a2) (b1). The dimension of the data vector is $N^d = 736$. The reconstruction domain $\mathcal{D}$ is a 10 cm $\times$ 10 cm $\times$ 10 cm cube, centered at (0, 0, 20 mm) and is discretized in $25 \times 25 \times 25$ cells with a cell size 4 mm, which yields 15625 permittivity unknowns.

The reconstruction with MS in Fig. 21 (a) smoothed the spheres. The individual spheres are better distinguished in Fig. 21 (b)-(d) with WCDA, where we used $\mu = 10^{-5}$. The permittivity of the spheres is somewhat underestimated with g_{l-h}. With g_{l-c} the edges are sharpest and the permittivities are close to the actual values apart from some smoothing that is visible between the spheres; a xz cross-section is shown in Fig. 22.

For comparison, the images from a full single-frequency data set at 8 GHz in Fig. 22 in [35] with Tikhonov regularization show rather well-shaped spheres but there are some fluctuations in their permittivity values. The contrast profiles from multi-frequency data in Fig. 27 of [36] with weighted L2 norm - TV regularization produce sharp edges and homogeneous permittivity values ($\varepsilon = 2.1$), though around the bottom some transitional values are visible. Sharp edges, with some artefacts, and homogeneous permittivity values ($\varepsilon \approx 2.4$) are obtained with SRVP regularization combined with extra *a priori* information in Figs. 14-15 in [15] from a full single-frequency dataset.

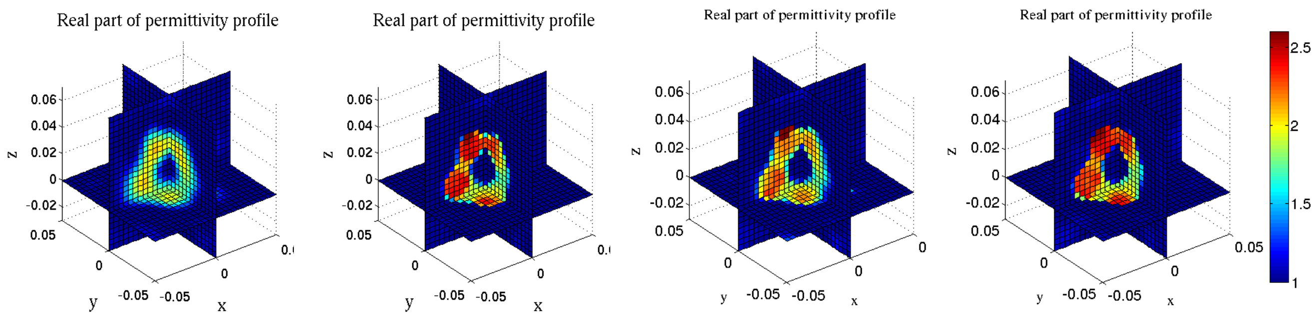

(a) MS (b) g_h (c) g_{l-h} (d) g_{l-c}

Figure 21. Real part of the complex permittivity for the *Myster* target. Reconstructions (using 736 data) from the sparsest antenna configuration (a2) (b1) of Fig. 13 at 8 GHz with: (a) MS, (b) g_h, (c) g_{l-h} and (d) g_{l-c}.

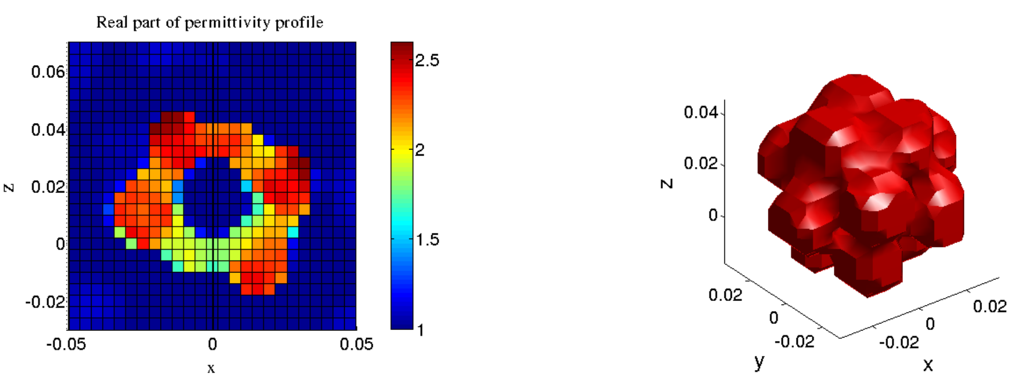

Figure 22. Cross section of g_{l-c} at $y = 0$ (left) and 3D iso-surface of the permittivity (right), corresponding to Fig. 21 (d).

7. Conclusion

In this paper, we presented a systematic study of WCDA models for regularizing the ill-posed nonlinear 3D electromagnetic inverse scattering problem. In particular, the properties of different models in this class were illustrated, and the choices of the interval parameter in these models and of the regularization parameter was optimized numerically for different complexity of objects, signal-to-noise ratios and subsampling antenna configurations. The focus was on 3D piecewise constant objects, where WCDA regularization appeared to be effective in reconstructing large numbers of unknowns from significantly smaller numbers of data, in both the simulated and experimental data cases. Different subsampling strategies were analyzed, resulting in a further improvement of computational efficiency.

Based on our analysis, the optimal regularization parameter μ appears to be sensitive to the SNR, while the optimal interval parameter γ remains quasi invariant and equal to approximately 0.01 for all three WCDA functions, under the different complexity of objects, SNR levels and antenna configurations considered in our study. The experiments confirmed that models that turn off the smoothing at large discontinuities (like g_{l-c} having Cauchy-Lorentzian in the tails) rather than allowing limited smoothing (like the Huber function g_h) indeed better preserve sharpness of the strong edges in the reconstructions. In terms of the reconstruction error, all the analyzed WCDA functions were similar, without clear dominance of one particular function.

References

[1] M. Pastorino. *Microwave Imaging.* Hoboken, John Wiley & Sons, 2010.

[2] D.W. Winters, J.D. Shea, P. Kosmas, B.D. Van Veen, and S.C. Hagness. Three-dimensional microwave breast imaging: dispersive dielectric properties estimation using patient-specific basis functions. *IEEE Trans. Med. Imaging*, 28(7):969 –981, july 2009.

[3] Q. Dong and C.M. Rappaport. Microwave subsurface imaging using direct finite-difference frequency-domain-based inversion. *IEEE Trans. Geosci. Remote Sensing*, 47(11):3664–3670, 2009.

[4] J.B. Detlefsen. Industrial applications of microwave imaging. In *Microwave Conference, 1991. 21st European*, volume 1, pages 108–119, 1991.

[5] J. Van Bladel. *Electromagnetic Fields.* Wiley-IEEE Press, 2007.

[6] W.C. Chew and Y.M. Wang. Reconstruction of two-dimensional permittivity distribution using the distorted Born iterative method. *IEEE Trans. Med. Imaging*, 9(2):218–225, 1990.

[7] N. Joachimowicz, C. Pichot, and J.P. Hugonin. Inverse scattering: an iterative numerical method for electromagnetic imaging. *IEEE Trans. Antennas Propag.*, 39(12):1742 –1753, dec 1991.

[8] A. Franchois and A. G. Tijhuis. A quasi-Newton reconstruction algorithm for a complex microwave imaging scanner environment. *Radio Sci.*, 38(2):VIC 12–1–VIC 12–13, 2003.

[9] T. M. Habashy and A. Abubakar. A general framework for constraint minimization for the inversion of electromagnetic measurements. *Progress In Electromagnetics*, 46:265–312, 2004.

[10] J. De Zaeytijd, A. Franchois, C. Eyraud, and J.-M. Geffrin. Full-wave three-dimensional microwave imaging with a regularized Gauss - Newton method - theory and experiment. *IEEE Trans. Antennas Propag.*, 55(11):3279 –3292, Nov. 2007.

[11] G. Demoment. Image reconstruction and restoration: overview of common estimation structures and problems. *IEEE Trans. Acoust., Speech, Signal Processing*, 37(12):2024 –2036, Dec 1989.

[12] A. Abubakar and P.M. Van Den Berg. Total variation as a multiplicative constraint for solving inverse problems. *IEEE Trans. Image Process.*, 10(9):1384 –1392, Sept. 2001.

[13] A. Abubakar, T.M. Habashy, Guangdong Pan, and Mao-Kun Li. Application of the multiplicative regularized Gauss - Newton algorithm for three-dimensional microwave imaging. *IEEE Trans. Antennas Propag.*, 60(5):2431–2441, 2012.

[14] P. Lobel, L. Blanc-Feraud, Ch. Pichot, and M. Barlaud. A new regularization scheme for inverse scattering. *Inverse Probl.*, 13(2):403, 1997.

[15] J. De Zaeytijd and A. Franchois. Three-dimensional quantitative microwave imaging from measured data with multiplicative smoothing and value picking regularization. *Inverse Probl.*, 25(2):024004, 2009.

[16] J. De Zaeytijd, A. Franchois, and J.M. Geffrin. A new value picking regularization strategy - application to the 3-D electromagnetic inverse scattering problem. *IEEE Trans. Antennas Propag.*, 57(4):1133 –1149, Apr. 2009.

[17] S. Van den Bulcke, A. Franchois, and D. De Zutter. Piecewise smoothed value picking regularization applied to 2D TM and TE inverse scattering. *IEEE Trans. Antennas Propag.*, 61(6):3261–3269, June 2013.

[18] S. Caorsi, G.L. Gragnani, S. Medicina, M. Pastorino, and G. Zunino. Microwave imaging based on a Markov random field model. *IEEE Trans. Antennas Propag.*, 42:293–303, Mar. 1994.

[19] A. Baussard, D. Prmel, and O. Venard. A Bayesian approach for solving inverse scattering from microwave laboratory-controlled data. *Inverse Problems*, 17(6):1659, 2001.

[20] F. Bai, A. Pižurica, S. Van Loocke, A. Franchois, D. De Zutter, and W. Philips. Quantitative microwave tomography from sparse measurements using a robust Huber regularizer. In *IEEE Int. Conf. Image Processing (ICIP)*, pages 2073–2076, Spet. 30 - Oct. 3, Orlando, Florida, USA, 2012.

[21] F. Bai, A. Pizurica, A. Franchois, S. Van Loocke, D. De Zutter, and W. Philips. Weakly convex discontinuity adaptive regularization for microwave imaging. *Antennas and Propagation, IEEE Transactions on*, 61(12):6242–6246, 2013.

[22] S. Z. Li. *Markov Random Field Modeling in Image Analysis*. Springer, 1995.

[23] J. M. Geffrin and P. Sabouroux. Continuing with the Fresnel database: experimental setup and improvements in 3D scattering measurements. *Inverse Probl.*, 25(2):024001, 2009.

[24] A. Litman and L. Crocco. Testing inversion algorithms against experimental data: 3D targets. *Inverse Probl.*, 25(2):020201, 2009.

[25] J. De Zaeytijd, I. Bogaert, and A. Franchois. An efficient hybrid MLFMA-FFT solver for the volume integral equation in case of sparse 3D inhomogeneous dielectric scatterers. *J. Comput. Phys.*, 227:7052–7068, July 2008.

[26] T. Hopkins and R. Dias da Cunha. The parallel iterative methods (PIM) package for the solution of systems of linear equations on parallel computers. Technical Report 19-94, University of Kent, Computing Laboratory, University of Kent, Canterbury, UK, September 1994.

[27] O.M. Bucci and T. Isernia. Electromagnetic inverse scattering: Retrievable information and measuement strategies. *Radio Science*, 32:2123–2137, 1997.

[28] A. Van den Bos. Complex gradient and Hessian. *Proc. Inst. Elect. Eng. Vision, Image Signal Process.*, 141(6):380–383, 1994.

[29] S. Z. Li. On discontinuity-adaptive smoothness priors in computer vision. *Pattern Analysis and Machine Intelligence, IEEE Transactions on*, 17(6):576–586, Jun 1995.

[30] S. Geman and D. Geman. Stochastic relaxation, Gibbs distributions, and the Bayesian restoration of images. *IEEE Trans. Pattern Anal. Mach. Intell.*, PAMI-6(6):721 –741, Nov. 1984.

[31] A. Blake and A. Zisserman. *Visual reconstruction*. MIT Press, Cambridge, MA, USA, 1987.

[32] M.J. Black, G. Sapiro, D.H. Marimont, and D. Heeger. Robust anisotropic diffusion. *Image Processing, IEEE Transactions on*, 7(3):421–432, Mar 1998.

[33] R.W. Cottle, J.S. Pang, and R.E. Stone. *The Linear Complementarity Problem*. Classics in applied mathematics. Society for Industrial and Applied Mathematics (SIAM, 3600 Market Street, Floor 6, Philadelphia, PA 19104), 1992.

[34] A. Capozzoli, C. Curcio, and A. Liseno. Gpu-based w - K tomographic processing by 1d non-uniform ffts. *Progress In Electromagnetics Research M*, 23:279–298, 2012.

[35] C. Yu, M. Yuan, and H. Liu. Reconstruction of 3D objects from multi-frequency experimental data with a fast DBIM-BCGS method. *Inverse Probl.*, 25(2):024007, 2009.

[36] M. Li, A. Abubakar, and P. M. van den Berg. Application of the multiplicative regularized contrast source inversion method on 3D experimental Fresnel data. *Inverse Problems*, 25(2):024006, 2009.

[37] C. Eyraud, A. Litman, A. Herique, and W. Kofman. Microwave imaging from experimental data within a Bayesian framework with realistic random noise. *Inverse Probl.*, 25(2):024005, 2009.

[38] I. Catapano, L. Crocco, M. D' Urso, and T. Isernia. 3D microwave imaging via preliminary support reconstruction: testing on the fresnel 2008 database. *Inverse Problems*, 25(2):024002, 2009.

[39] P. C. Chaumet and K. Belkebir. Three-dimensional reconstruction from real data using a conjugate gradient-coupled dipole method. *Inverse Probl.*, 25(2):024003, 2009.